A multi-parameter field monitoring system to investigate the dynamics of large earth slides–earth flows in the Northern Apennines, Italy

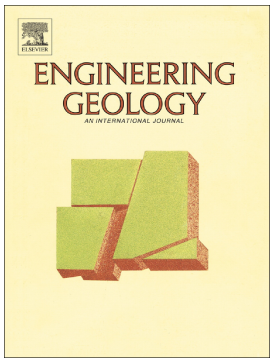

A multi-parameter field monitoring system to investigate the dynamics of large earth slides–earth flows in the Northern Apennines, Italy

Alessandro Chelli, Roberto Francese, Emma Petrella, Andrea Carri, Andrea Quagliarini, Andrea Segalini, Maria Pia Caporicci, Michela Diena, Massimo Giorgi, Fulvio Celico

PII: S0013-7952(19)31345-6

DOI: https://doi.org/10.1016/j.enggeo.2020.105780

Reference: ENGEO 105780

To appear in: *Engineering Geology*

Received date: 8 July 2019

Revised date: 22 July 2020

Accepted date: 22 July 2020

Please cite this article as: A. Chelli, R. Francese, E. Petrella, et al., A multi-parameter field monitoring system to investigate the dynamics of large earth slides–earth flows in the Northern Apennines, Italy, *Engineering Geology* (2019), https://doi.org/10.1016/j.enggeo.2020.105780

A multi-parameter field monitoring system to investigate the dynamics of large earth slides–earth flows in the Northern Apennines, Italy

Alessandro Chelli[1,5,*], Roberto Francese[1,2,5], Emma Petrella[1,5], Andrea Carri[3], Andrea Quagliarini[1], Andrea Segalini[3], Maria Pia Caporicci[1], Michela Diena[4], Massimo Giorgi[2], Fulvio Celico[1,5]

[1] Department of Chemistry, Life Sciences and Environmental Sustainability, University of Parma, Parco Area delle Scienze 157/A, 43124, Parma, Italy

[2] National Institute of Oceanography and Experimental Geophysics – OGS, Borgo Grotta Gigante 42/C, 34010, Sgonico, Trieste, Italy

[3] Department of Engineering and Architecture, University of Parma, Parco Area delle Scienze 181/A, 43124, Parma, Italy

[4] Agenzia per la Sicurezza Territoriale e la Protezione Civile, Emilia Romagna Region Administration, Servizio Area Affluenti Po, Strada Garibaldi 75, 43100, Parma, Italy

[5].Centre for Energy and Environment-CEE/CIDEA, University of Parma, Parco Area delle Scienze, Podere Campagna, 43124,Parma, Italy

* Corresponding author: alessandro.chelli@unipr.it, +39 521 905 334

http://orcid.org/0000-0001-5035-733X

Abstract

Large earth slides and rocks lides evolving into earth flows are quite widespread in the Northern Italian Apennines. Despite being simply referred to as landslides, many of them are, in fact, large complexes of landslides. They evolved through multiple and/or successive movements, undergoing partial and/or total reactivations. The reactivation of pre-existing landslide bodies is the prevalent

mechanism for the known landslide events, as the historical records and the technical reports indicate. Landslide reactivation is, indeed, a relevant topic from the perspective of risk assessment and mitigation.

A multi-parameter monitoring system was installed on a large complex of landslides that underwent partial or total reactivations after heavy rainfall events, causing damages to buildings and infrastructures. Two clusters of automatic piezometers—each coupled with an inclinometer—and a time-lapse resistivity deployment were the core of the monitoring system. A weather station, collecting data from subsurface thermometers, and a water content probe completed the system.

After the construction of a new geological model of the slope, this study aimed at understanding the possible mechanisms leading to the reactivation of the landslide. This goal was achieved by gaining insights into the process of rainfall infiltration into the landslide deposits, by determining the groundwater flow and evaluating the landslide displacements.

The monitoring system captured the processes that took place in the landslide bodies and the bedrock in response to a rainfall event in early February 2017, which followed a dry period of eight months. The recorded data provided indications on the variation of the hydraulic head in the groundwater within the landslide and the bedrock, particularly at the sliding surfaces. The electrical conductivity of the groundwater and the resistivity of the terrain varied across the failure surfaces. In particular, a sudden increase in the electrical conductivity was related to the locations of the main sliding surfaces. The joint analysis of time-lapse resistivity, hydraulic heads, and groundwater electrical conductivity helped to identify the locations of weaker levels within the landslide masses, which were confirmed by data from inclinometers.

This study improved the knowledge of the hydrogeological behaviour of a complex of landslides in heterogeneous low-permeability media. Moreover, the obtained results contributed to the understanding of the role played by different portions of the landslide complex in the evolution of the movement.

Keywords: large earth slide–earth flow, landslide reactivation, hydrogeology, geophysics, Northern Italian Apennines.

1. INTRODUCTION

Landslides significantly contribute to the evolution of landforms in hilly and mountainous areas (Korup, 2009; Crozier, 2010; Korup et al., 2010; Bell et al., 2012). In this framework, if they are of sufficient magnitude and size (Guthrie and Evans, 2007), they can also act as formative processes (i.e., they may shape landforms that persist in the landscape).

Most of the slopes in the Northern Italian Apennines are affected by landslides, which involve wide portions of the territory of the mountain chain. In the portion of Apennines in the Emilia Romagna region, on the Adriatic side of the mountain belt, the landslide inventory map (Regione Emilia-Romagna 2012) indicates that landslides cover up to 20% of the mountainous area. This percentage rises to 50% in the territory of some municipalities. Many of these landslides are large and complex earth slides or rock slides evolving into earth flows. When they occur adjacent to one another, they form a typical landslide-related landscape (Bertolini et al., 2017).

Even though they are referred to as landslides, many of them are actually large complexes of landslides that developed during the Holocene and, in some cases, since the Late Pleistocene (Bertoldi et al., 2007; Bertolini, 2007; Bertolini and Tellini, 2001; Soldati et al., 2006). They often affect areas of 10^4–10^5 m^2 and displace volumes in the order of 10^7–10^8 m^3. The lithology and structure of the bedrock are among the predisposing factors for these large landslides (Bertolini and Pellegrini, 2001). The tectonics in the Northern Italian Apennines also play a major role in the development of faults and thrusts, which represent weak zones together with the associated sets of fractures. Furthermore, tectonics controls the recent uplift that has conditioned a large part of the geomorphological evolution of the slopes (Carlini et al., 2018). The complexes of landslides evolved through multiple and/or successive movements, undergoing partial and/or total reactivations.

Rainfall is the main factor triggering these reactivations, especially during autumn and spring when precipitation events can last for several days. Recent climate changes are influencing the

distribution of rainfall (Jongman et al., 2014) and the alternation of prolonged dry periods and intense rainfall is becoming fairly common.

The reactivation of pre-existing landslides is the prevalent mechanism characterising hundreds of landslide events, as the historical records and recent technical reports indicate. First-time failures are, on the other hand, much rarer (Bertolini et al., 2017). The occurrence of reactivation is a relevant topic from the perspective of risk assessment and mitigation. Since the 9th century, landslide reactivations affected and damaged villages which were built on top of landslide bodies, as reported in historical archives (Regione Emilia-Romagna, 2014). In some cases, the same archives allow to roughly assess the return periods of these reactivations, which range from decades to centuries. Owing to the relatively long periods during which these landslides were dormant, the topographic surfaces shaped by these processes were considered suitable for human settlement and agriculture as they exhibited smaller steepness and milder landforms compared to the surroundings.

Although large earth slide–earth flows are connected to the stream network (as they could reach the valley bottoms), reactivations are often not influenced by fluvial erosion as demonstrated by their prevalent origin far from the landslide toe. The reactivation of these landslides includes mechanism such as (a) failures at the crown zone, (b) undrained loading of pre-existing landslide deposits, and (c) downslope failure propagation of the entire landslide body (Bertolini and Pizziolo, 2008).

The Case Pennetta landslide, an earth/rock slide–earth flow named after the nearest settlement, is part of a large complex of landslides and has been investigated since early 2016. An integrated monitoring system was designed and was associated to surface observations to assess the landslide kinematics as well as the subsurface water flow paths. Additional goals included the assessment of water infiltration, which in such a low-permeability and heterogeneous media had a significant influence on the landslide movement. The multi-parameter monitoring system is composed of two inclinometers, three piezometric gathers, and two electrical resistivity spreads (TL_ERT). It also features a rain gauge equipped with air and ground thermometers and water content probes.

This study was aimed at understanding the possible mechanisms leading to the reactivation of the landslides. The goal was achieved by gaining insights into different processes, such as the rainfall infiltration in the landslide deposits, the determination of the groundwater flow (from measured variations in the electrical/physical properties of the subsurface materials), and the occurrence of displacements. Understanding the relationships among the processes affecting different portions of the complex of landslides was another broader aim of the study.

Within the framework of a long-term study of the area of interest, this study primarily focused on 1) developing the landslide geological model, also useful to properly design the monitoring system, and 2) exploring ways to correlate datasets of groundwater electrical conductivity, terrain resistivity, groundwater heads, and displacements to define the failure surfaces of the landslide and its internal dynamics.

2 MATERIALS AND METHODS

2.1 General setting of the landslide

The Case Pennetta landslide occurred on the left flank of the valley of the Taro River, one of the main streams in this part of the Northern Apennines. The top of the slope is at about 700 m a.s.l., while its foot lies at about 250 m a.s.l., at the bottom of the valley (Fig. 1).

The annual mean temperature is 12.4 °C (reference period 1991–2015; Antolini et al., 2017). From September 2016 to September 2017, the total amount of precipitation (460 mm) was influenced by a few events. This amount is low when compared to the annual mean precipitation, which equals to 938 mm (reference period 1991–2015; Antolini et al., 2017).

Rocks outcropping in the study area belong to three distinct tectonic units (Fig. 1) of the Northern Italian Apennines (Vescovi ed., 2002), a folded and thrusted mountainous range that has been developing since the Cenozoic (Boccaletti et al., 1971; Kligfield, 1979; Vai and Martini, 2001; Molli, 2008 and references therein). The formation of *Arenarie di Scabiazza* (SCB) occupies the top

of the slope and is composed of thin layers of black to grey claystone alternating with 15–20 cm thick layers of sandstone that gradually turn into thin to very thin sandstone layers, and finally to marls. This formation lies stratigraphically on the *Argille a Palombini di Monte Rizzone* (AMR), composed of claystone and dm-size beds of limestone (calcilutites). These rocks belong to the *Media Val Taro* tectonic unit. In some places, AMR disappears and SCB lies directly on the *Ottone* tectonic unit. The latter, locally composed of dark grey claystone containing clasts and blocks of whitish to pale brown limestone (*Argille a blocchi*, CCVb), lies directly on the *Flysch of Monte Caio* (CAO) (with tectonic contact), made by thick beds of marly-limestone turbidites intercalated with thin to medium beds of dark argillite. All these rocks are deeply tectonised.

Steep surfaces and scarps generally characterise the lower portion of the slope (Fig. 1), where the thick beds of CAO outcrop. Landforms are smooth and mild in the upper portion of the slope, where claystone (AMR, CCVb) constitutes the prevailing lithology, and the landslides have caused abrupt changes in the topographic gradient.

The Case Pennetta landslide suffered important reactivations (http://geo.regione.emilia-romagna.it/schede/fs/fs_dis.jsp?id=1207s7) in 1997, 1992, 1927, and 1916, and also in 1900, even though scarce information exists on this event. The most recent total reactivation occurred in April 2001, following some localised movements in the crown in October–November 2000. During this event, similar to that in 1927, the landslide reached the main road (SS 308) at the bottom of the Taro valley as well as the Parma–La Spezia railway. Similar events occurred in 1916 and probably, also in 1900. The Parma–La Spezia railway is an important infrastructure of a major commercial corridor across the Apennines, connecting the Mediterranean Sea with the Brennero Pass in the Alps, and thus, with Central and Northern Europe. After the 2001 event, an inclinometer was installed in correspondence of the crown of the Case Pennetta landslide. Data were recorded only for a few months, and the sensor became non-operational soon after 2007. Since 2010, people living in the area started to note visible effects of slope instability, such as cracks and fissures on the

ground surface and changes in the slope shape. They also reported damages to buildings, such as tilting of the floors and microcracks in the walls.

The movement rate of the Case Pennetta landslide, according to recent history, ranges from extremely slow to very slow (Cruden and Varnes, 1996) for most of the time, with seldom total reactivations.

2.2 Electrical Resistivity Tomography

Electrical Resistivity Tomography (ERT) has been a valuable tool to constrain and improve the geological model of the site and gain an initial insight into the electrical properties of the terrain. ERT was also used to monitor changes in the subsurface properties. Standard surveying was associated with innovative and new-generation multi-source measurements. The latter technique is particularly effective in focusing the electrical field, thus increasing the resolution of the larger dipoles (Picotti et al., 2017).

The resistivity profiles L and MS were collected to test the response of the slope material and aid in the geological and geomorphological interpretation of the landslide (Fig. 2a).

The top of line L was placed at approximately 710 m a.s.l., upslope of the Case Pennetta settlement, while its bottom was located at about 505 m a.s.l., near Case Costa. The line crossed the whole upper part of the complex of landslides. Data were collected using a 48-electrode IRIS Syscal Pro georesistivimeter capable of sampling the potential from 10 channels simultaneously, thereby reducing the field effort. This system delivers a maximum voltage of 800 V, providing an adequate signal-to-noise ratio at very large transmitter apertures and in fairly conductive terrains. The electrode spacing was set to 5.0 m and a roll-along scheme with 50% overlap was chosen for the acquisition. A 0.9 km profile (Fig. 2a) was then covered with a base sequence and 6 roll-along sequences. A Wenner configuration with two additional pole–dipole arrays were used in each segment, resulting in a dataset of ~18,000 data points.

The line MS was collected transversely to the slope, few tens of metres west of Case Pennetta (Fig. 2a). The topography along the profile gently dips eastwards. This line investigated the portion of the complex of landslides located upslope of the Case Pennetta site.

Data along this second profile were collected using a multi-phase technology multi-source (MS) georesistivimeter. The MS system (LaBrecque et al., 2013) is comprised of a series of stand-alone transceivers with timing synchronised via a GPS signal. The MS system is new-concept instrument capable of injecting current simultaneously through multiple dipoles connected to different transceivers. Along the profile, 7 units were deployed with electrode spacing set to 10.0 m, for a total length of 0.2 km. The dipole-dipole array with additional inline poles was the recording choice.

The reliability of the two datasets was confirmed by reciprocal measurements, which exhibited only a minor deviation. A few noisy data points, probably caused by poor electrode coupling, were removed from the dataset. Three-dimensional resistivity images were then generated via iterative inversion of the field data. The smoothness-constrained approach (Constable et al., 1987), associated with a careful reweight of the inversion parameters (Morelli and LaBrecque, 1996), was preferred and it provided better results. Cells with large DOI (Depth of Investigations) values (Oldenburg and Li, 1999) were discarded.

The resistivity profiles ER11 and ERT2 (Fig. 2b) were incorporated in the monitoring system of the Case Pennetta landslide. They include two fixed arrays of 48 channels, each of them composed of buried electrodes spaced 5.0 m apart, deployed and set up to provide daily resistivity sections. The acquisition array was a Wenner alpha, and data processing was carried out similarly to the previous datasets.

Time-lapse resistivity images were corrected for temperature fluctuations (Hayley et al., 2007) using data collected from thermometers installed in a borehole at depths of 2.0 m, 4.0 m, and 6.0 m,

hosted nearby the meteorological station. The ground temperature was measured using TT-N NESA sensors.

2.3 Hydrogeological investigation

Two multilevel groundwater monitoring systems (cluster type) were installed to measure the hydraulic head at different depths within the heterogeneous medium. Cluster A comprised two multilevel piezometers (A1 and A2), whereas cluster B included three multilevel piezometers (B1, B2, and B3). Between the two clusters, a single piezometer (C1) was installed. Details of these piezometers are reported in Table 1, and their position is visible in Fig. 2b.

The hydraulic head in each of the six piezometers was measured hourly using a pressure transducer with a data-logger (STS DL.OCS/N/RS485).

The electrical conductivity (EC) of the groundwater was measured monthly with a borehole probe (SOLINST TLC) to analyse possible haloclines and investigate the hydrogeological behaviour of the heterogeneous medium (Morin et al., 1997; Cook et al., 1999; Petrella et al., 2009; Aquino et al., 2015). Measurements were carried out at depth intervals of 1 m. The reliability of the EC values was always verified through laboratory analyses.

2.4 Geological investigation and inclinometers

A total of 8 boreholes were drilled in the landslide area, along an NNW–SSE alignment, to provide subsurface geological information and collect core samples to analyse. Stratigraphy was reconstructed at SI1 and SI2 (Table 1), equipped with inclinometers, whereas A1, A2, B1, B2, B3, and C1 were used as piezometers (Table 1 and Fig. 2b), as reported above.

The borehole stratigraphy at the old inclinometer, located 2 m apart from SI1, was also available along with a first indication of the depth of the failure plane.

Standard penetration tests (SPT) were conducted while drilling SI1 and SI2 on levels of particular interest. Several core samples were collected and specific geotechnical tests were carried out at different laboratories of the Interregional Agency of the Po River (AIPo).

The site was instrumented with two manual inclinometers, SI1 and SI2 (Fig. 2b), installed between late January and early February 2016. The main goal was to detect failure planes and assess the horizontal displacements. Another objective of the study was to test the overall performances of a traditional monitoring approach, in order to consider the possible installation of an automatic monitoring system. SI1, located near cluster A (Fig. 2b; Table 1), reached a depth of 35 m and monitors the crown of the Case Pennetta landslide. SI2, located near cluster B (Fig. 2b; Table 1), reached a depth of 30.5 m and monitors the head of the landslide. The zero reading of both inclinometers was taken on 15th March 2016. The sampling period was approximately a month and the readings were taken every 0.5 m.

3 RESULTS

3.1 Geological and geomorphological features of the Case Pennetta landslide

The landslide extends from 650 to 265 m a.s.l. for a length of ~1600 m and a maximum width of ~130 m (Fig. 1).

The geomorphological map highlighted that the crown of the Case Pennetta landslide actually corresponds to another landslide belonging to the complex of landslides, characterising the entire slope. The well-developed main scarp, featuring a concave longitudinal topographic profile, and the surface of the head, clearly in counter-slope, account for a typical rotational movement (Fig. 1; Fig. 2a).

This behaviour affects the depleted mass of the landslide that extends down to the elevation of 510 m a.s.l., where the toe of the failure surface is masked by the materials accumulated at the foot. In fact, earth flows start from the front of the depleted mass and reach the Taro River, flowing along a creek channel.

The part of the landslide with rotational kinematics affects the SCB formation and also, marginally, the AMR formation.

SI1 (Fig. 2b; Fig. 11 c) shows, down to the depth of 30–31 m (616–615 m a.s.l.), a matrix-supported deposit characterised by the presence of a clay-silty matrix, and clasts and blocks of variable sizes (from 0.5 to 10–12 cm). From 31 to 34 m depth, the deposit changes to clast-supported, and is composed of breccia, poorer in matrix compared to the upper portion. The top of the bedrock was encountered at about 35 m depth (612 m a.s.l.). In the intervals 6–9 m and 11–14 m below the ground surface (b.g.s.), the landslide deposit shows an alternation of compact and loose levels, the latter characterised by a certain degree of disaggregation. Materials from 21–23 m b.g.s. appear to be more disaggregated.

SI2 (Fig. 2b; Fig. 11 c) shows, between the ground surface and 20 m b.g.s., a deposit made by clasts and blocks of different sizes (from grains to pebbles) with abundant silty-clay matrix. The larger blocks are seldom gathered in correspondence to specific depth intervals, such as those between 7 and 10 m b.g.s. or in the first 3 m b.g.s. A level richer in clay material has been observed at 14–15 m b.g.s. Dispersed organic material has also been found in the first 20 m of coring.

Between 20 and 23 m b.g.s., the features of the deposit change. It is generally clast-supported, made of a silty sandy clay matrix with abundant clasts from gravel to blocks (up to 10 cm). Between 21 and 21.5 m b.g.s., the matrix is more abundant than in the other portion of this depth interval. At 23 m b.g.s. (561 m a.s.l.), the rock appears to be made by thin layers of black to grey claystone and grey sandstone (SCB).

A sieve analysis showed relevant percentages of silt (30–50%) in the landslide mass, and the Atterberg limits allowed to classify the fine-grained soil composition as ‘CL – Inorganic clays of low to medium plasticity’, as defined by the Unified Soil Classification System (USCS). The undrained cohesion was measured with pocket tests and free lateral expansion tests, and a mean

value of 127.8 kPa was obtained. Direct shear tests carried out with a Casagrande shear box indicate a range of friction angles between 16° and 23°.

3.2 Electrical Resistivity Tomography

3.2.1 Exploration profiles L and MS

The longitudinal profile L crosses major geological boundaries (Fig. 3). These boundaries have a sharp response also in the resistivity image. A major resistive body is imaged in the upper part of the section, with values ranging from 40 to 80 Ω·m, and moving towards the Case Pennetta settlement, the terrain resistivity decreases to 20–25 Ω·m down to an elevation of approximately 640 m a.s.l.

The profile in this segment is already located in the landslide area (LSL), and available boreholes and trenches show the presence of an abundant clay matrix, justifying such low values. The in-depth resistivity increases again to values of 35–40 Ω·m, marking a change in physical properties of the subsurface.

The resistivity values increase to 80–100 Ω·m along the landslide scarp located just downslope of Case Pennetta. The in-depth resistivity decreases again to values below 30 Ω·m. Moving down along the slope, the resistivity remains below 40 Ω·m from the base of the scarp to the edge of the gently dipping surface located south of the scarp. Then, it increases again to values of approximately 80–100 Ω·m where Scabiazza sandstone (SCB) bedrock outcrops are present. In the final segment of the profile, an abrupt contact is found between the relatively resistive SCB and the highly conductive Palombini claystone (AMR).

The transversal profile MS is mostly located in the landslide area. The resistivity is fairly low and ranges between 20 Ω·m and 40 Ω·m (Fig. 3). In the western segment and the uppermost layers, the values are larger, whereas they decrease to 20 Ω·m at a depth of 10–12 m below the surface. In the

eastern segment, the resistivity is approximately 20–25 Ω·m and is roughly the same in the near-surface and deeper layers.

3.2.2 Time-lapse resistivity measurements

Two major rainfall events occurred within the period of geophysical monitoring (1st July 2016 – 31st May 2017). The first one occurred in October 2016 with a cumulative rainfall of 55 mm in two days. The second one, with a cumulative rainfall of 45 mm in six days, occurred from 30th January to 4th February 2017 (Fig. 4). Owing to the small amount of rainfall, changes in subsurface resistivity during the two events were marginal and slightly similar (around 2–3 Ω·m) although the February event appears to be more representative because a larger number of resistivity lapses was collected. The reference for the February event is a resistivity section recorded during the last days of January 2017 (Fig. 5). The terrain resistivity in the first three days after the rainfall only exhibited minor changes right within the range of the experimental error (Fig. 5). The section recorded on 8th February shows a moderate increase in the resistivity in the very shallow layers. The behaviour becomes more evident in the sections collected on 9th February and 10th February. The fringe of increased resistivity progresses in-depth down to ~10 m below the surface, whereas the resistivity decreases again in the uppermost layers. The hydraulic head in the C1 piezometer was found at ~12 m below the surface, indicating a thick unsaturated zone characterised by vertical infiltration. The resistivity in the layers at depths larger than 10 m began to decrease 4–5 days after the end of the rainfall. The reduced amount of water infiltrating into the subsurface could not lead to further correlations between changes of resistivity and rainfall.

3.3 Hydrogeological behaviour

Measurements of groundwater level in the upper cluster (A) clearly show a significant vertical difference between the hydraulic heads of A1 and A2 (Fig. 6a). The shallower piezometer (A2) shows several peaks during winter due to different infiltration events, suggesting rapid percolation of water from the ground surface towards the phreatic surface. In contrast, the deeper piezometer

(A1) shows a smoothed hydrograph and a delayed response in terms of head increase compared with the hydrograph recorded in A2.

No relevant head differences were detected in the lower cluster (B), taking the topographic error into account (Fig. 6b). The hydrographs are the same in all three piezometers. The main head increase is delayed compared to that observed in A2, in agreement with the heterogeneity of the studied medium.

A rapid response of the hydraulic head to infiltration events is also observed in C1 (Fig. 6c). The head increase is consistent with those recorded in A2.

The EC varies significantly with depth. The shallower piezometers (A2, B3, and C1) show groundwater EC variations over time, strictly related to local precipitation (Figs. 4, 6d, 6e, and 6f). Therefore, in the shallow saturated zone, these EC variations depend on two factors, namely the effective infiltration of local rainwater, and the mixing between lower-salinity fresh infiltration water and higher-salinity pre-event groundwater.

In A2 (Fig. 6d), the EC shows a large difference between the value recorded in the lower section of the piezometer, higher than 4000 μS/cm, and that measured in the upper section of the piezometer, i.e. ~1000 μS/cm. A 'staircase shape' is visible (Fig. 6d) and the EC steps were always detected at the same depth. Taking into consideration the features of A2 (Table 1) and the variation of the hydraulic head at a depth within a heterogeneous medium, the progressive evolution could be partially influenced by intra-well mixing.

Within cluster B (Fig. 6e) also, the EC exhibits a large difference between the value recorded in the lower section of B3 (higher than 5000 μS/cm) and that measured in the upper sections of B2 and B1 (slightly higher than 1500 μS/cm). On the contrary, slight differences were observed between the values in the lower section of B2 and those in the upper section of B1. In the latter, the EC slightly and progressively increases with depth, up to approximately 2000 μS/cm.

In piezometer C1 (Fig. 6f) also, the EC varies with depth, but the variations are less evident when compared with those observed in the other shallow piezometers (A2 and B3). The values recorded in the lower section of the piezometer is always lower than 2400 μS/cm, while the values recorded in the upper section range from 900 μS/cm (in March) to 2150 μS/cm (at the end of October).

3.4 Inclinometers

The inclinometer SI1 (Table 1, Fig. 2b) recorded 37.9 mm of cumulated displacement (Fig. 7b) over a period of 26 months. The major local movements are identifiable at depths of 33–34 m b.g.s. (612.3–613.3 m a.s.l.) and 22–23 m b.g.s., with a maximum local displacement of 6.6 and 13.1 mm, respectively (Fig. 7a). Additionally, the last available measures show a minor local displacement of 2.6 mm at 25 m depth (621.3 m a.s.l.). Until the last available recording (11th June 2018), the monthly average velocity at a depth of 22.5 m (623.3 m a.s.l.) exhibited a constant value of 0.016 mm/day.

The inclinometer SI2, over the same period, recorded 18.3 mm of cumulated displacement (Fig. 8a). The major local movements are identifiable at 14.5–15 m depth (576.4–576.9 m a.s.l.) with a secondary minor sliding surface at 6.5 m depth (584.9 m a.s.l.). The maximum displacements are 1.5, 2.3, and 1.6 mm, respectively (Fig. 8b), while the major superficial movement reached 2.3 mm (1.5 m depth, 589.9 m a.s.l.). The presence of the earth flow at the landslide toe is another factor that plays a significant role in the overall behaviour observed in the SI2 area.

From the beginning of the monitoring activity to the end of January 2018, major local displacements recorded at SI1 show a linear trend with a coefficient of determination between 0.870 and 0.986, with a mean value of 0.947 corresponding to a constant velocity. With this simple interpretative model, it is possible to identify changes in the velocity trend representing a potential hazard. An example of this application is reported in Fig. 9, where the behaviour until 30th January 2018 is compared with the last two available readings. There is significant divergence from this

trend at 22.5 m and 22 m depth (623.8 and 624.3 m a.s.l., respectively), whereas the last two data values related to the depth of 23 m (623.3 m a.s.l.) are consistent with the past trend.

In the case of SI2, the behaviour is quite different and does not follow a linear trend. In particular, the non-linear pattern indicates a decrease of velocity during the monitoring period, suggesting a more stable condition in this area. It should also be noted that local displacement values recorded at SI2 are considerably lower compared to those at SI1.

4 DISCUSSION

4.1 Refined geological and geotechnical model of the landslide

By using the data obtained from the aforementioned investigations, it was possible to define the model of the landslides, identifying three different portions of the monitored slope (Fig. 11a). In the part of the complex of landslides located upslope from the Case Pennetta landslide (I in Fig. 11a, 650–700 m a.s.l.), the outcropping bedrock is composed of SCB, and the landslides are constrained in-depth at SI1, where they extend down to 34 m b.g.s. The SI1 inclinometer accounts for the presence of sliding surfaces in the depth intervals 22–23 and 33–34 m b.g.s. The ERT profiles L and MS contributed to define the landslides as mainly composed of claystone, and sandstone pieces and blocks, indirectly extending the material observed in correspondence of SI1 (Fig. 11c).

As suggested by the rates of movement recorded by SI1 (Fig. 7), the deformation shows the characteristics of a slow secondary creep (Cruden and Varnes, 1996) occurring along the sliding surfaces marked by an increase in terrain resistivity (Fig. 3), which seem almost parallel to the slope topography below Case Pennetta.

The existence of a relatively less resistive portion in the slope suggests the presence of crushed and homogenised landslide material, where clasts of different sizes are dispersed in a matrix. On the other hand, relatively more resistive portions are representative of materials with a lower degree of fragmentation including rock blocks (La Penna et al., 2005). These are identified as different rock

masses detached from the original slope, such as in correspondence to the main scarp of the Case Pennetta landslide, which probably comprises a large rock block detached from the bedrock. This model supports the hypothesis of a rotational rock/earth slide–earth flow with complex behaviour.

The differences in hydraulic head values, as well as the different head variations observed over time between piezometers A1 and A2, suggest the presence of a hydraulic discontinuity (e.g., a very low-permeability horizon) between the upper and the lower saturated zone, at least locally. At the same time, a significant difference in bulk permeability is expected between the medium overlying the said low-permeability horizon and that underlying the same horizon. As a matter of fact, owing to the combination of these hydraulic features, (i) the two aquifer portions can be recharged by different areas, with different hydraulic head upgradient, and (ii) the hydraulic gradient can be different, therefore causing different head losses along the groundwater pathway. The shallower piezometer (A2) is strongly affected by individual rainfall events; this is clearly due to the small thickness of the local unsaturated zone and drying cracks. Moreover, as demonstrated in recent works, the percolation of fresh-infiltration waters within the shallow unsaturated zone is not negligible (Rizzo et al., 2020) and enhanced by local arthropods (Remelli et al., 2019), which can increase both the effective porosity and the permeability of the upper medium.

The second portion (II in Fig. 11a; roughly 600–650 m a.s.l.) is the higher part of the Case Pennetta earth/rock slide. It is characterised by a high scarp with a planform concave shape just downslope of the cluster A and SI1 (Fig. 11). This landform represents the main scarp of a rotational rock/earth slide that is mainly masked by successive collapses of material, as revealed by its longitudinal topographic profile (Fig. 11). As testified by the relatively high resistivity values, the landslide material in correspondence to the main scarp is matrix-supported, with abundant to very abundant rock pieces (see description of SI1). It could also be a large portion of a rock that did not completely lose its coherence.

Downslope from the scarp, an almost flat surface represents the head of the Case Pennetta landslide. The borehole data (SI2) allowed to constrain the thickness of the landslide body to ~23 m b.g.s. Materials are quite similar to those collected from SI1, and they appear disaggregated at different depths. The level around 14–15 m b.g.s., rich in clay material, corresponds to the depth where most of the movement, even if of a low entity, has been observed (Fig. 8). Movements recorded in this area by the inclinometer SI2 show variations over time probably influenced by the rotational nature of the movement.

The substantial agreement among the hydraulic heads measured at different depths suggests that all the aquifer portions investigated through the cluster B are recharged by a unique area with a same hydraulic head upgradient, and/or the net groundwater flow and the local shape of the equipotential lines are mainly influenced by the vicinity of the local groundwater delivery (Fig. 11a).

The jump in EC values observed at cluster B suggests the existence of a continuous low-permeability horizon, which hinders the hydraulic interconnection between the upper (landslide mass) and the lower (SCB bedrock) portions of the investigated saturated zone.

On the whole, the distribution of the EC values with depth seems to be related to (i) different residence time within higher- and lower-permeability aquifer portions, corresponding to higher or lower water-rock interactions and therefore, higher or lower mineral dissolution, and/or (ii) the interaction between groundwater and different minerals characterised by different solubility.

The third portion (III in Fig. 11a, 540–600 m a.s.l.) corresponds to a steep slope segment featuring a succession of flat (seldom in counter slope) and steep surfaces (Fig. 11a). This portion of the Case Pennetta landslide is characterised by several collapsed ‘blocks’ (rock blocks/pieces and earth) displaced by rotational movement. Earth flow phenomena, composing the last part of the landslide, originate from these collapsed blocks.

4.2 Response to rainfall

Time-lapse (TL) geophysical imaging clearly shows (Fig. 5), as expected in low-permeability terrains, that moderate rainfall mostly affects the resistivity field in the uppermost layers. The February 2017 rainfall event appears to be more representative as the reference profile was collected about a week before the rainfall, and evapotranspiration during the winter in cohesive soils and at such elevations is close to zero (Xu and Singh, 2001). In such conditions, changes in resistivity depends only on the seepage determined by rainfall and the variation of seepage water chemistry. Although anomalous infiltration paths caused by surface fissures (Gance et al., 2015) were supposed to be negligible in wintertime, the anomalous season caused some drying cracks that were partially open during the monitoring period. Rainfall occurred over six days, from 30th January to 4th February 2017, for a total of 45 mm.

The changes in the resistivity field observed in the first lapse (Fig. 5), computed from 24th January to 8th February, developed in two layers: (i) the uppermost layer (A in Fig. 5) in which the resistivity decreased by ~3–5% and (ii) the lower layer in which the resistivity increased by 5–6% (B in Fig. 5). This increase is caused by the vertical infiltration of rainwater. The rainwater is more resistive compared to the groundwater (according to the observations made in terms of EC variations in the shallower groundwater during rainfall), and infiltration in the uppermost layer progresses as a 'plane wavefront' whose geometry is controlled by hydraulic conductivity. Rapid infiltration of rainwater (supported by the hydraulic head measurements in the shallow piezometers) causes the resistivity to increase at the front of the infiltration wave, whereas it progressively decreases at the tail of the infiltration wave resulting in the rapid groundwater ion enrichment occurring in clayey terrains (Schwartz et al., 2008).

Changes in resistivity in the second lapse (Fig. 5), computed from 8th February to 9th February, are less than 0.5–1.0%, both positive and negative. Such amount of change is within the inversion error and is therefore negligible. The situation could be then considered stationary, and vertical infiltration does not occur anymore.

The third lapse was computed from 9th February to 10th February (Fig. 5). Two sectors of major changes are visible in the resistivity image. In the first spot (C in Fig. 5), the resistivity decreases by approximately 2–3% at 20–25 m below the surface. The delay between rainfall and resistivity changes in depth is comparable to that observed in the piezometers. In the second spot (D in Fig. 5), the resistivity decreases by ~4% right in the uppermost layer. In this area, the electrode line crosses a small creek, and the decrease of resistivity is probably caused by prolonged infiltration of rainwater flowing along the creek itself.

A direct comparison, at the borehole location, of the different monitoring datasets provided additional insights for the interpretation of the subsurface parameters. A comprehensive set of measurements from the boreholes and the surface was available for the mid of May 2017. At piezometer C1 (Fig. 12), right in the middle of the resistivity line ERT2 during the lapse time, the groundwater table was located approximately 13 m b.g.s. The EC of the groundwater (Fig. 12) changes rapidly from 1200 μS/m to 2400 μS/m just 1 m below the water table and remains rather constant down to the borehole bottom. The resistivity (extracted from the monitoring line ERT2) in the unsaturated zone increases up to 36–37 Ω·m in the uppermost layer (Fig. 12) and remains rather constant down to approximately 3 m b.g.s. The water table in the resistivity profile is visible as it is marked by an inflection point of the resistivity curve. The resistivity at larger depths drops to 27 Ω·m. The change in groundwater EC affects the resistivity curves only marginally, probably because the subsurface is mostly comprised of cohesive terrains with low porosity.

At cluster A (Fig. 13), during the lapse time, the water table was located ~3 m b.g.s. The displacement log (Fig. 13) clearly shows two sliding surfaces at 22.5 m and 34.0 m below the surface. The groundwater EC (Fig. 13) increases rapidly from 1000 μS/m to over 3500 μS/m in the uppermost 5 m (3–8 m b.g.s.) of the aquifer. Then, the conductivity remains rather constant for the next 5 m (8–13 m b.g.s.) but steps up again to over 4000 μS/m at 18 m b.g.s. The terrain resistivity (extracted from the ERT L profile) is approximately consistent with the groundwater EC, as the

resistivity curve is roughly mirrored (Fig. 13). In the unsaturated zone, the resistivity rapidly decreases from 60 Ω·m to ~30 Ω·m. The terrain resistivity below the groundwater table keeps decreasing down to a depth of 13 m, where it begins to increase again, reaching 23 Ω·m at large depths. The deeper step in groundwater EC is not sensed in the terrain resistivity curve, and the reason seems to be the same as that described for piezometer C1. The uppermost sliding surface appears to be marked in the terrain resistivity curve by the presence of an inflection point located exactly 22.5 m b.g.s. This change probably outlines a small difference in the degree of compaction within the landslide deposits.

At cluster B (Fig. 14), during the lapse time, the groundwater table was located approximately 9 m b.g.s. The displacement log (Fig. 14) shows a secondary sliding surface 14.5 m b.g.s. The groundwater EC (Fig. 14) clearly shows two different domains. In the shallower aquifer (B3), except for the uppermost 2 m (where it is influenced by the mixing with fresh infiltration waters), it exhibits values larger than 5000 μS/m (down to 15 m b.g.s.), while in the deeper aquifers (B1 e B2), it is significantly lower and gently increases from 1500 μS/m (at 20–22 m b.g.s.) to ~2000 μS/m (at 34 m b.g.s.). The sliding surface is located right in between the shallower saturated horizon investigated through piezometer B3, and the deeper horizon investigated through piezometers B1 and B2, suggesting how the displacement, crushing the clay layers, could have partly sealed the deeper aquifer causing the observed difference in groundwater EC.

The major changes in subsurface parameters, despite the short monitoring period, show a good correspondence among the different datasets. In the part I of the slope (Fig. 11a), the correlation between the failure plane (Fig. 7) and the subtle changes in electrical resistivity in the part C (Fig. 5) is noteworthy. All these results lead to consider the depth interval between 623 m a.s.l. and 625 m a.s.l. as a significant variation in the monitored properties. These were contemplated as a response to the amount of rainfall received during the February event. Indeed, changes in subsurface parameters permit to highlight the presence of failure surfaces and, in general, weakness

surfaces within the landslide masses. This might contribute to the understanding of the mechanisms occurring at the slope scale immediately before a reactivation, which, in these large landslides, is a product of undrained loading (Hutchinson and Bhandari, 1971), as reported also in several other cases in this area (Bertolini and Pizziolo, 2008).

A better comparison of the monitored parameters could be achieved by completely automating the system and synchronising the sampling rate. This would result in an effective description of the ongoing phenomenon and could give the possibility of implementing time-of-failure forecast and threshold assessment methods (e.g., Segalini et al., 2018).

The occurrence of rainfall of limited intensity, within a dry period, probably allowed to observe better and greater details of the changes that occurred within the landslide mass. Besides, the increase in velocity of the landslide movement (Fig. 3) means that these changes had both a short and medium term influence on the dynamics of the upper part of the slope that represent the crown of the Case Pennetta landslide.

5 CONCLUSIONS

The comprehensive approach applied to the study of the complex of landslides and the Case Pennetta landslide, in particular, resulted in a new and reliable geological model of the entire slope. Field surveys and geophysical measurements constrained the geometry of the sliding surfaces. The resistivity of the landslide materials is 50% lower compared to that of the underlying bedrock. The slope comprises three distinct portions with distinctive kinematics, separated from each other by discontinuity surfaces.

The landslide response to rainfall events, despite the small amount of precipitation, was recorded in the monitored parameters. EC of groundwater and terrain resistivity showed relevant changes across the failure surfaces in both monitored portions of the slope. Particularly, the sudden increase in the electrical conductivity of the groundwater observed in the area of the rotational slide seems to be

related to the main sliding surface. This could be an effect of the displacement itself, locally sealing the deeper aquifer.

The joint analysis of time-lapse resistivity, hydraulic heads, and groundwater EC could then suggest the position of levels of weaknesses within the landslide mass. The analysis of inclinometer data confirmed this.

In a broader context, the present study allowed to refine the knowledge about the hydrogeological behaviour within a complex of landslides in heterogeneous low-permeability media. As a matter of fact, the combination of hydraulic head and EC measurements in multilevel piezometers depicts the following scenario:

- The hydraulic head can significantly vary with depth within the saturated medium;
- The distribution of the hydraulic head within both the heterogeneous landslide and the underlying bedrock can be influenced by (i) very low permeability sliding surfaces within the landslide mass, and/or (ii) the vicinity of a relatively narrow groundwater delivery that causes the whole groundwater (flowing within the landslide and the underlying bedrock) to flow towards a common 'point' (Fig. 11);
- From the hydrogeological point of view, sliding surfaces can behave as low- or no-flow boundaries.
    - The sliding surface located between the screened intervals of piezometers A1 and A2 behaves as a no-flow layer, considering (i) the different hydraulic heads, (ii) the different head variations over time, and (iii) the different EC with depth.
    - However, the near-vertical tracts of the sliding surfaces located between the rock masses investigated through clusters A and B must behave as a low-flow boundary because (i) no springs were detected at the interception between this surface and the ground (therefore, the groundwater flowing upgradient must flow through it, towards the mass downgradient), but (ii) the hydraulic gradient must increase within the same sliding horizon.

In the perspective of future works, it is not yet completely clear how the rotational slide dynamics influence the earth flow located in the downslope portion. Besides, the response of the dynamics of the slopes to the distribution of rainfall related to climate change deserves to be investigated.

The multi-parametric approach needs to be further implemented and improved. Manual reading of some of the monitored parameters is time-consuming, and the sampling frequency is too low for statistical analyses and proper modelling of risk scenarios. For this reason, it would be advisable to automate the instrumentation and guarantee a higher and homogeneous data acquisition frequency. Moreover, these features could allow the implementation of more advanced models, including predictive and early warning methodologies, which need higher sampling frequency to provide reliable results.

The experimented approach has a significant potential to be transferable to other landslides. The knowledge of landslide dynamics in these heterogeneous and low-permeability materials is a major contribution to the hazard assessment and risk mitigation, regarding the occurrence of landslide reactivations also in other geological contexts where similar conditions exist.

Acknowledgements

The present work is supported by the Agency of Civil Protection – Emilia Romagna Region Administration, by local funds of the University of Parma (CHELLFIL12; FILCHELLI14 Head: A. Chelli), and by the National Institute of Oceanography and Experimental Geophysics – University of Parma research agreement (Heads: A. Chelli, R. Francese). This work has besides benefited from the framework of the COMP-HUB Initiative, funded by the 'Departments of Excellence' program of the Italian Ministry for Education, University and Research (MIUR, 2018-2022). We are grateful to the Editor-in-Chief, Dr. Janusz Wasowski, and the three anonymous reviewers for their suggestions, which greatly improved the manuscript and the figures.

References

Antolini G, Pavan V, Tomozeiu R, Marletto V (2017) Atlante climatico dell'Emilia Romagna 1961-2015. Arpae Emilia-Romagna Servizio IdroMeteoClima pp. 31

Aquino D, Petrella E, Florio T, Celico P, Celico F (2015) Complex hydraulic interactions between compartmentalized carbonate aquifers and heterogeneous siliciclastic successions: a case study in southern Italy. Hydrological Processes, 29:4252-4263

Bell R, Petschko H, Röhrs M, Dix, A, (2012) Assessment of landslide age, landslide persistence and human impact using airborne laser scanning digital terrain models. Geografiska Annaler, Series A, Physical Geography, 94: 135–156 doi:10.1111/j.1468-0459.2012.00454.x

Bertoldi R, Chelli A, Roma R, Tellini C (2007) New data from Northern Apennines (Italy) pollen sequences spanning the last 30,000 yrs. Alpine and Mediterranean Quaternary 20(1):3-20

Bertolini G, (2007) Radiocarbon dating on landslides in the Northern Apennines (Italy). In: McInnes R, Jakeways J, Fairbank H, Mathie E (eds) Landslide and Climate Changes: challenges and solutions. Proceedings of the International Conference on Landslides and Climate Change, Ventnor, Isle of Wight, UK, 21–24 May 2007. Taylor & Francis Group, London, pp 73–80

Bertolini G, Corsini A, Tellini C (2017) Fingerprints of Large-Scale Landslides in the Landscape of the Emilia Apennines. In: Soldati M and Marchetti M (eds) Landscapes and Landforms of Italy. World Geomorphological Landscapes Springer Cham pp 215-224

Bertolini G, Pellegrini M (2001) The landslides of Emilia Apennines (northern Italy) with reference to those which resumed activity in the 1994-1999 period and required civil protection interventions. Quaderni di Geologia Applicata 8(1):27–74

Bertolini G, Pizziolo M, (2008) Risk assessment strategies for the reactivation of earth flows in the Northern Apennines (Italy). Engineering Geology 102(3–4):178–192

Bertolini G, Tellini C, (2001) New radiocarbon dating for landslide occurrences in the Emilia Apennines (Northern Italy). Trans Japan Geom Un 22(4):C-23

BoccalettiM, Elter P, Guazzone G, (1971) Plate tectonic model for the development of the Western Alps and Northern Apennines. Nature 234:108–110

Carlini M, Chelli A, Francese R, Giacomelli S, Giorgi M, Quagliarini A, Carpena A, Tellini C (2018) Landslides types controlled by tectonics-induced evolution of valley slopes (Northern Apennines, Italy). Landslides 15(2):283-296

Constable SC, Parker RL, Constable CG (1987) Occam'sOccam's inversion: A praticalpractical algorithm for generating Constable smooth models from electromagnetic sounding data. Geophysics, 52:289-300

Cook PG, Love AJ, Dighton JC (1999) Inferring groundwater flow in fractured rock from dissolved radon. Ground Water 37:606–610

Crozier MJ, (2010) Landslide geomorphology: An argument for recognition, with examples from New Zealand. Geomorphology, 120: 3–15.

Cruden DM, Varnes DJ (1996) Landslide types and processes. In: Turner AK, Shuster RL (eds) Landslides: investigation and mitigation, Transportation Research Board, National Research Council, special report, vol 247. National Academy Press, Washington DC, pp 36–75

Gance J, Sailhac P, Malet JP (2015) Corrections of surface fissure effect on apparent resistivity measurements. Geophys. J. Int. 200: 1118–1135

Guthrie RH, Evans SG, (2007) Work, persistence, and formative events: the geomorphic impact of landslides. Geomorphology, 88: 266–275

Hayley K, Bentley LR, Gharibi M, Nightingale M (2007) Low temperature dependence of electrical resistivity: Implications for near surface geophysical monitoring. Geophysical Research Letters 34:L18402. doi: 10.1029/2007GL031124

Hutchinson JN, Bhandari RK, (1971) Undrained loading, a fundamental mechanism of mudflows and other mass movements. Geotechnique, 21 (4): 353–358

Jongman B, Hochrainer-Stigler S, Feyen L, Aerts JCJH., Mechler R, Botzen WJW, Bouwer LM, Pflug G, Rojas R, Ward PJ (2014) Increasing stress on disaster-risk finance due to large floods. Nat. Clim. Change, 4:264–268

Kligfield R, (1979) The Northern Apennines as a collisional orogen. Am. J. Sci. 279:676–691

Korup O, (2009) Linking landslides, hillslope erosion, and landscape evolution. Earth Surface Processes and Landforms, 34: 1315–1317

Korup O, Densmore AL, Schlunegger F, (2010) The role of landslides in mountain range evolution. Geomorphology, 120: 77–90.

LaBrecque DJ, Morelli G, Fischanger F, Lamoureux P and Brigham R (2013) Field trials of the multi-source approach for resistivity and induced polarization data acquisition. In: Proceedings of the 2013 AGU Fall Meeting, American Geophysical Union, abstract NS34A-03, December 9–13, San Francisco.

La Penna V, Lorenzo P, Perrone A, Piscitelli S, Rizzo E, Sdao F (2005) Case history: 2D electrical resistivity imaging of some complex landslides in Lucanian Apennine (Southern Italy). Geophysics 70(3):11-18

Molli G (2008) Northern Apennines-Corsica orogenic system: an updated overview. The Geological Society of London Special Publication 298(1):413-442

Morelli G, LaBrecque DJ (1996) Advances in ERT inverse modeling, Europ. J. Environ. Eng. Geophys., 1(2):171–186.

Morin RH, Carleton GB, Poirier S (1997) Fractured-aquifer hydrogeology from geophysical logs; the Passaic Formation, New Jersey. Ground Water 35:328–338

Oldenburg DW, Li Y (1999) Estimating depth of investigation in dc resistivity and IP surveys. Geophysics 64(2):403–416

Petrella E, Naclerio G, Falasca A, Bucci A, Capuano P, De Felice V, Celico F (2009) Non-permanent shallow halocline in a fractured carbonate aquifer, southern Italy. Journal of Hydrology 373:267-272

Picotti S, Francese, R, Giorgi, M, Pettenati, F and Carcione, JM (2017) Estimation of glacier thicknesses and basal properties using the horizontal-to-vertical component spectral ratio (HVSR) technique from passive seismic data, J. Glaciol., 63(238), 229–248

Regione Emilia-Romagna (2012) Landslide characteristics in Emilia-Romagna. Regione Emilia-Romagna. https://ambiente.regione.emilia-romagna.it/it/geologia/geologia/dissesto-idrogeologico/le-caratteristiche-dei-fenomeni-franosi-in-emilia-romagna

Regione Emilia-Romagna (2014) Historical archive of landslide events. Regione Emilia-Romagna. https://ambiente.regione.emilia-romagna.it/it/geologia/geologia/dissesto-idrogeologico/larchivio-storico-dei-movimenti-franosi

Remelli S, Petrella E, Chelli A, Conti FD, Fondón CL, Celico F, Francese R and Menta C (2019) Hydrodynamic and Soil Biodiversity Characterization in an Active Landslide. Water 11, 1882; doi:10.3390/w11091882.

Rizzo P, Petrella E, Bucci A, Salvioli Mariani E, Chelli A, Sanangelantoni AM, Raimondo M, Quagliarini A, Celico F (2020) Studying hydraulic interconnections in low-permeability media by using bacterial communities as natural tracers. Water 12, 1795; doi: 10.3390/w12061795.

Schwartz, B. F., M. E. Schreiber, and T. Yan (2008) Quantifying field-scale soil moisture using electrical resistivity imaging. J. Hydrol. 362(3–4):234–246. doi:10.1016/j.jhydrol.2008.08.027

Segalini A, Valletta A, Carri A (2018) Landslide time-of-failure forecast and alert threshold assessment: A generalized criterion. Engineering Geology 245,72-80

Soldati M, Borgatti L, Cavallin A, De Amicis M, Frigerio S, Giardino M, Mortara G, Pellegrini GB, Ravazzi C, Surian N, Tellini C, Zanchi A, Alberto W, Albanese D, Chelli A, Corsini A, Marchetti M, Palomba M, Panizza M (2006) Geomorphological evolution of slopes and climate changes in northern Italy during the Late Quaternary: spatial and temporal distribution of landslides in Northern Italy and landscape sensitivity implications. Geografia Fisica e Dinamica Quaternaria, 29, 165-183, ISSN: 0391-9838

Vai GB, Martini IP (2001) Anatomy of an Orogen: The Apennines and Adjacent Mediterranean Basins. Kluver Academic Publisher, Dordrecht/Boston/London.

Vescovi P ed, (2002) Note illustrative della Carta Geologica d'Italia alla scala 1:50.000. Foglio 216 Borgo Val di Taro. Servizio Geologico d'Italia-Regione Emilia Romagna, pp. 115 pp

Xu C.Y. and Singh V.P. (2001) Evaluation and generalization of temperature-based methods for calculating evaporation. Hydrological Processes 15(2):305–319

Figure captions and table headings

Figure 1.

Geomorphological sketch map of the considered complex of landslides: a) active and b) dormant landslide scarp; c) active and d) dormant rotational and/or translational landslide; e) active and f) dormant earth flow; g) the Case Pennetta landslide is highlighted with red background; h) debris/earth flow cone with man interventions; i) main thrust. SCB: Arenarie di Scabiazza (sandstone); AMR: Argillle a Palombini di Monte Rizzoli (claystone); CCVb: Argille a blocchi (claystone with blocks); CAO: Flysch of Monte Cassio (marly-limestone). The area shown in Fig. 2a is pointed out on the picture. Base map: Technical Regional Map 1:5000, Emilia-Romagna Region 1998 (ed.).

Figure 2.

The sketch map focuses on the part of the landslide where the monitoring system was realised: a) geomorphology and geophysical exploration lines ERTL (NNW–SSE) and ERTMS (ENE–WNW); trace of the cross-section of Fig. 10a is also reported; b) detail of the monitoring system; the represented area is enclosed in the white square traced in the part (a) of the figure; keys: M1: meteorological station equipped with borehole thermometers; A_i, B_i, C_i: piezometer; SI_i: borehole and inclinometer; ERTi: resistivity deployment for time-lapse measurements.

Figure 3.

Resistivity profiles ERTL (longer one) and ERTMS. SCB: Scabiazza sandstones; LSL: landslide deposits; AMR: Argille a Palombini claystone.

Figure 4.

a) Cumulative rainfall recorded by the Case Pennetta weather station up to the last available data, obtained on 30th March 2017; b) cumulative rainfall of the October 2016 event; c) cumulative rainfall of the January–February 2017 event.

Figure 5.

Inverse model resistivity (left) of data collected before the rainfall event (24th January 2017) and immediately after the rainfall event (8–10 February 2017) along the ERT2 resistivity line. Percentage changes in terrain resistivity (right) computed between the different lapses. Letters A, B, C, and D are described in the text.

Figure 6.

Example of groundwater level fluctuations vs. rainfall (boxes a, b, and c; in box b, there is a 1-month detail to show the difference in hydraulic head between B1, B2, and B3), and vertical profile of the electrical conductivity recorded in the upper Cluster A, the lower Cluster B, the C1 piezometer (boxes d, e, and f, respectively).

Figure 7.

a) Local and b) cumulative displacements recorded by the SI1 inclinometer from the beginning of the monitoring activity.

Figure 8.

a) Local and b) cumulative displacements recorded by the SI2 inclinometer from the beginning of the monitoring activity.

Figure 9.

Local displacement versus time for the SI1 inclinometer at different depths compared to a linear regression model.

Figure 10.

Local displacement versus time for the SI2 inclinometer at different depths compared to a linear regression model.

Figure 11.

a) Cross-section along the profile of Fig. 2a showing the geological model of the upper portion of the Case Pennetta landslide as revealed by the joint and integrated analysis of the available data collected over time; active landslides are in red and the dormant portion of the landslide is in pale yellow; the piezometers B1, B2, and B3 are not represented in their exact positions (see Fig. 2b) to show the relationship among them and the sliding surfaces; the water table, groundwater flow directions, and equipotential lines are drawn for the low flow period; b) piezometers installed in the slope with the indication of the screened (dotted line) parts; c) sketch representation of the stratigraphy in SI1 and SI2.

Figure 12.

(a) Variation of the groundwater electrical conductivity measured in the piezometer C1, and (b) terrain resistivity measured with ERT2.

Figure 13.

(a) Variation of the landslide local displacements recorded in SI1, (b) groundwater electrical conductivity measured in the piezometer A2, and (c) terrain resistivity measured with ERT-L.

Figure 14.

(a) Variation of the landslide local displacements recorded in SI2, and (b) groundwater electrical conductivity measured in the piezometers of cluster B.

Table 1 Coring and boreholes carried out for this study and types of devices installed. The depths are measured below the ground surface (b.g.s.), and the elevation above sea level (a.s.l.).

Alessandro Chelli Conceptualization, Methodology, Data curation, Writing- Original draft preparation, Writing- Reviewing and Editing, Project administration, Funding acquisition, Supervision

Roberto Francese Conceptualization, Methodology, Data curation, Writing- Original draft preparation, Writing- Reviewing and Editing, Project administration, Funding acquisition

Emma Petrella Conceptualization, Methodology, Data curation, Writing- Original draft preparation, Writing- Reviewing and Editing, Project administration

Andrea Carri Data curation, Writing- Original draft preparation, Investigation

Andrea Quagliarini Investigation

Andrea Segalini Conceptualization, Methodology, Data curation, Writing- Original draft preparation, Writing- Reviewing and Editing, Project administration

Maria Pia Caporicci Software

Michela Diena Funding acquisition

Massimo Giorgi Investigation

Fulvio Celico Conceptualization, Methodology, Data curation, Writing- Original draft preparation, Writing- Reviewing and Editing, Project administration, Funding acquisition, Supervision

Borehole	UTM (m) 32 T	Elevation of ground surface (m a.s.l.)	Maximum depth (m b.g.s.)	Screened interval (m bgs/m a.s.l.)	Type of device
SI1	573643.7E 4938449.99N	646.3	35		Inclinometer
SI2	573729.64E 4938306.14N	595.5	30		Inclinometer
A1	573633.03E 4938457.35N	646.0	35	30-35/616-611	Piezometer
A2	573630.58E 4938459.47N	646.1	25	1-25/645-621	Piezometer
B1	573731.82E 4938306.8N	591	35	30-35/55[illegible]-55[illegible]	Piezometer
B2	573733.52E 4938306.92N	591	23	20-23/[illegible]69-566	Piezometer
B3	573735.14E 4938307.79N	591	15	3-15/586-574	Piezometer
C1	573753.34E 4938408.75N	610.5	2[illegible]	3-20/605-588	Piezometer

Table 1

Declaration of interests

☒ The authors declare that they have no known competing financial interests or personal relationships that could have appeared to influence the work reported in this paper.

☐The authors declare the following financial interests/personal relationships which may be considered as potential competing interests:

Highlights:

Dynamics of earth slides-earth flows within a complex of landslides.

Time-varying resistivity and borehole water conductivity reveal landslide activity

Increase in the electrical conductivity of groundwater is related to sliding surfaces

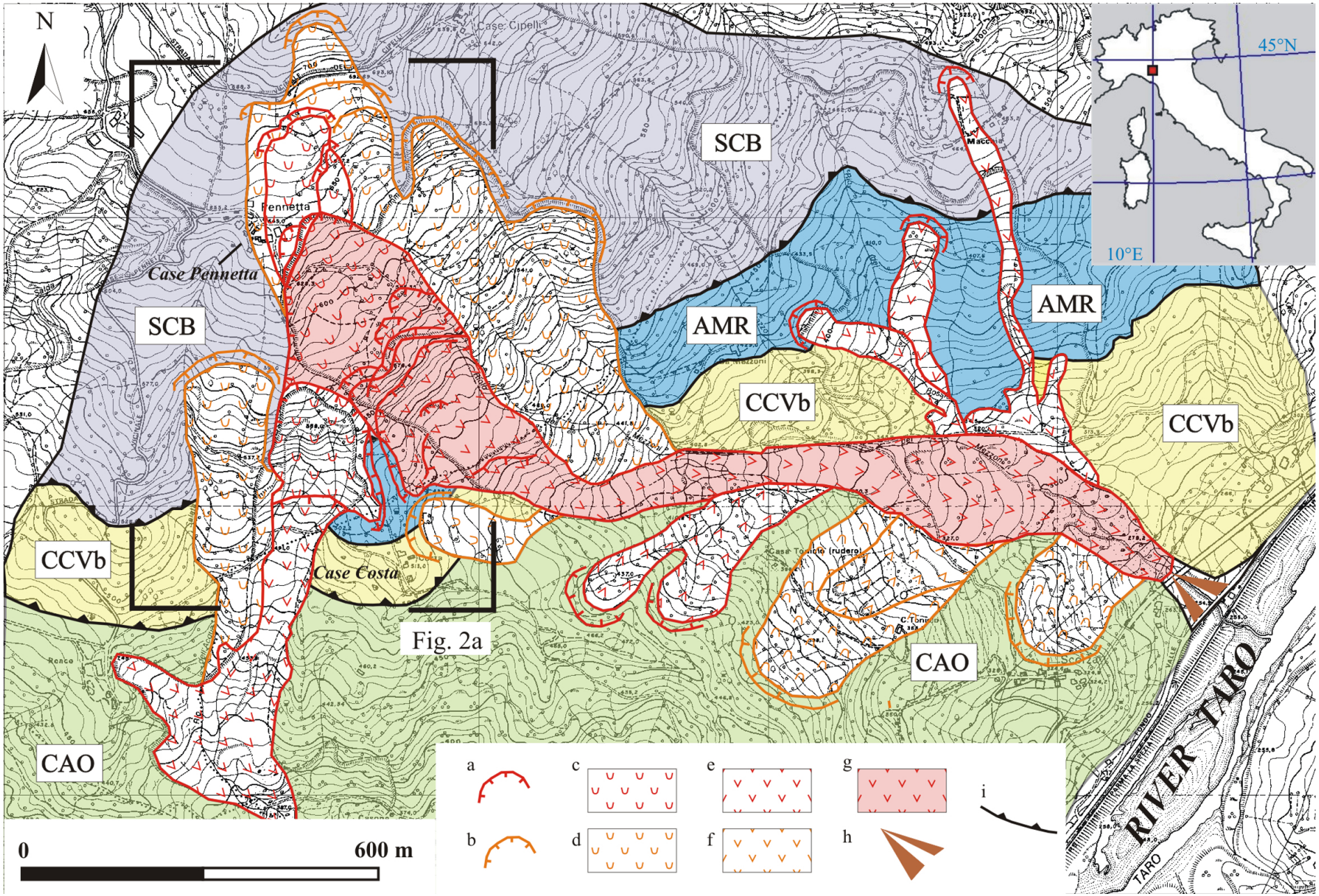
N
SCB
AMR
CCVb
CAO
Case Pennetta
Case Costa
Fig. 2a
0
600 m
45°N
10°E
RIVER TARO
a
b
c
d
e
f
g
h
i

Figure 1

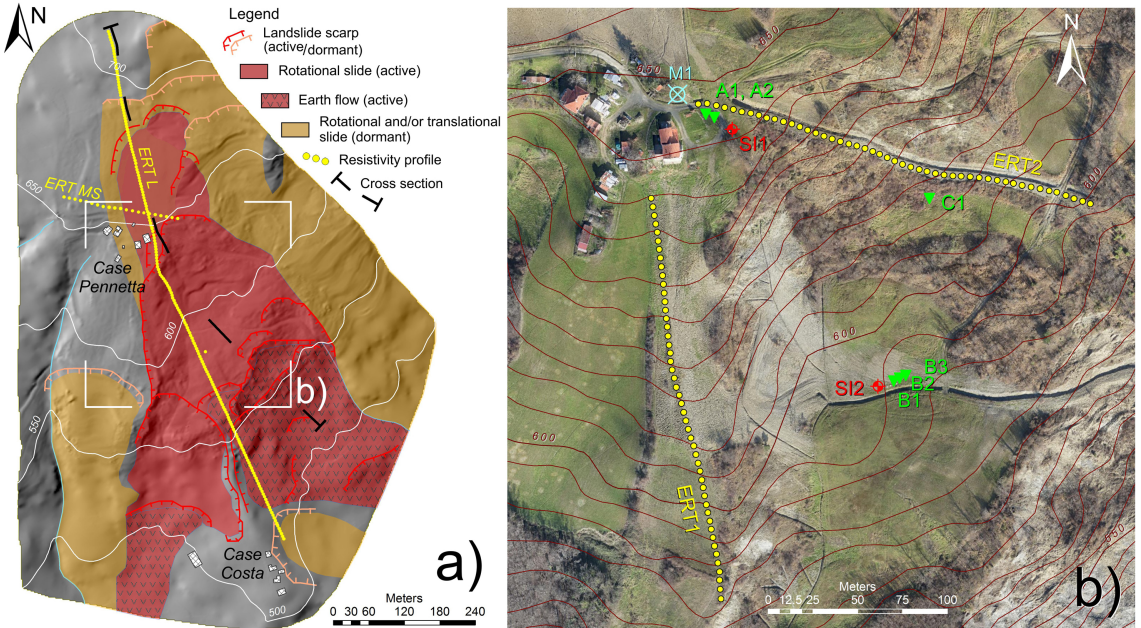
N
Legend
Landslide scarp (active/dormant)
Rotational slide (active)
Earth flow (active)
Rotational and/or translational slide (dormant)
Resistivity profile
Cross section
ERT MS
ERT L
Case Pennetta
Case Costa
b)
a)
Meters
0 30 60 120 180 240
M1
A1, A2
SI1
ERT2
C1
SI2
B3
B2
B1
ERT1
N
Meters
0 12.5 25 50 75 100
b)

Figure 2

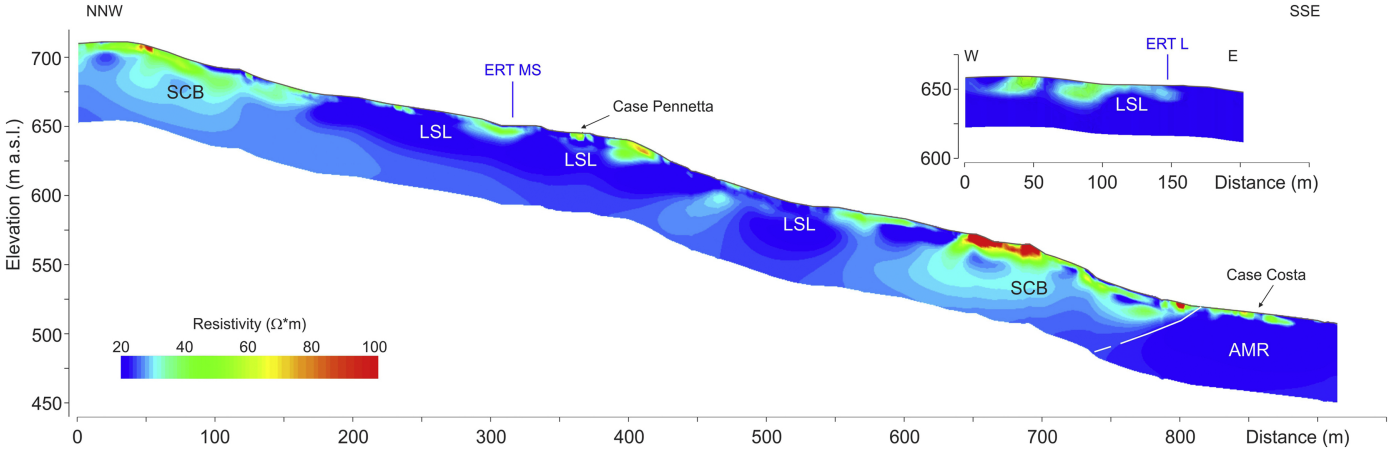
NNW
SSE
ERT MS
Case Pennetta
ERT L
W
E
SCB
LSL
LSL
LSL
LSL
SCB
AMR
Case Costa
Resistivity (Ω*m)
20
40
60
80
100
Elevation (m a.s.l.)
700
650
600
550
500
450
0
100
200
300
400
500
600
700
800
Distance (m)
650
600
0
50
100
150
Distance (m)

Figure 3

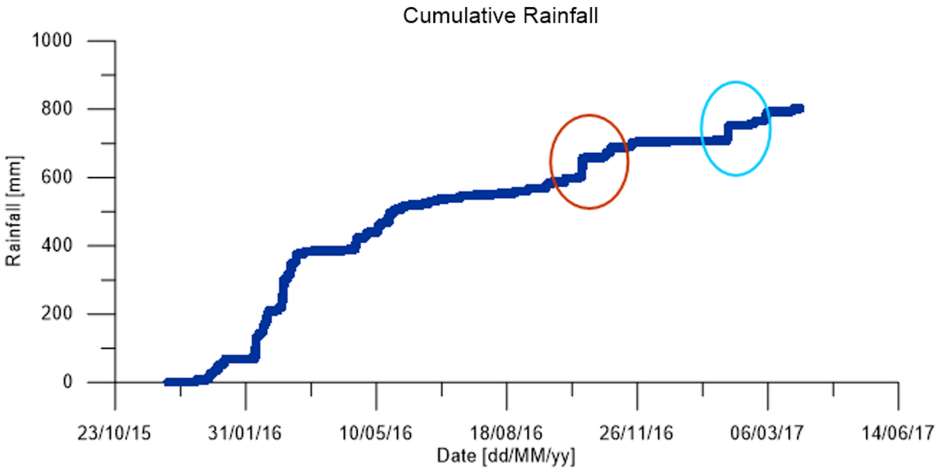
Cumulative Rainfall
Rainfall [mm]
1000
800
600
400
200
0
23/10/15
31/01/16
10/05/16
18/08/16
26/11/16
06/03/17
14/06/17
Date [dd/MM/yy]

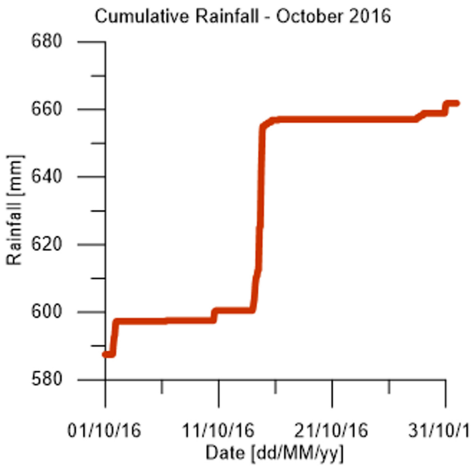
Cumulative Rainfall - October 2016
Rainfall [mm]
680
660
640
620
600
580
01/10/16
11/10/16
21/10/16
31/10/16
Date [dd/MM/yy]

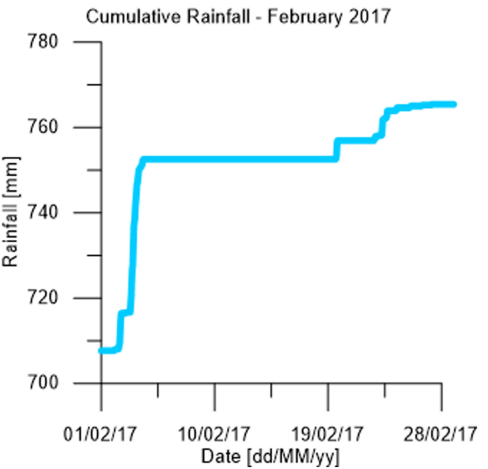
Cumulative Rainfall - February 2017
Rainfall [mm]
780
760
740
720
700
01/02/17
10/02/17
19/02/17
28/02/17
Date [dd/MM/yy]

Figure 4

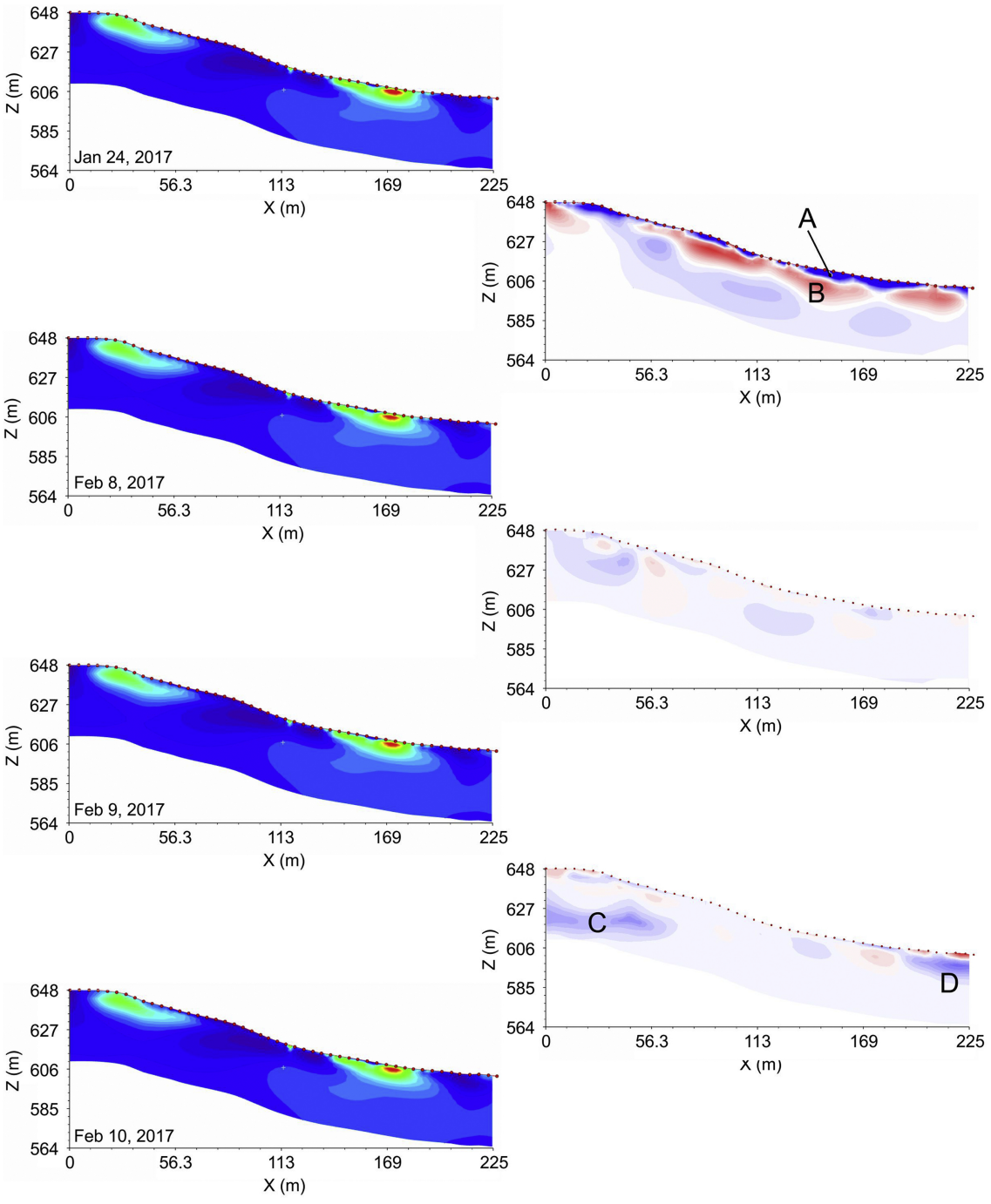
Z (m)
X (m)
Jan 24, 2017
Feb 8, 2017
Feb 9, 2017
Feb 10, 2017
A
B
C
D
Resistivity (Ωm)
10.0
26.3
42.5
58.8
75.0
Resistivity changes (%)
-5.00
-2.50
0.00
+2.50
+5.00

Figure 5

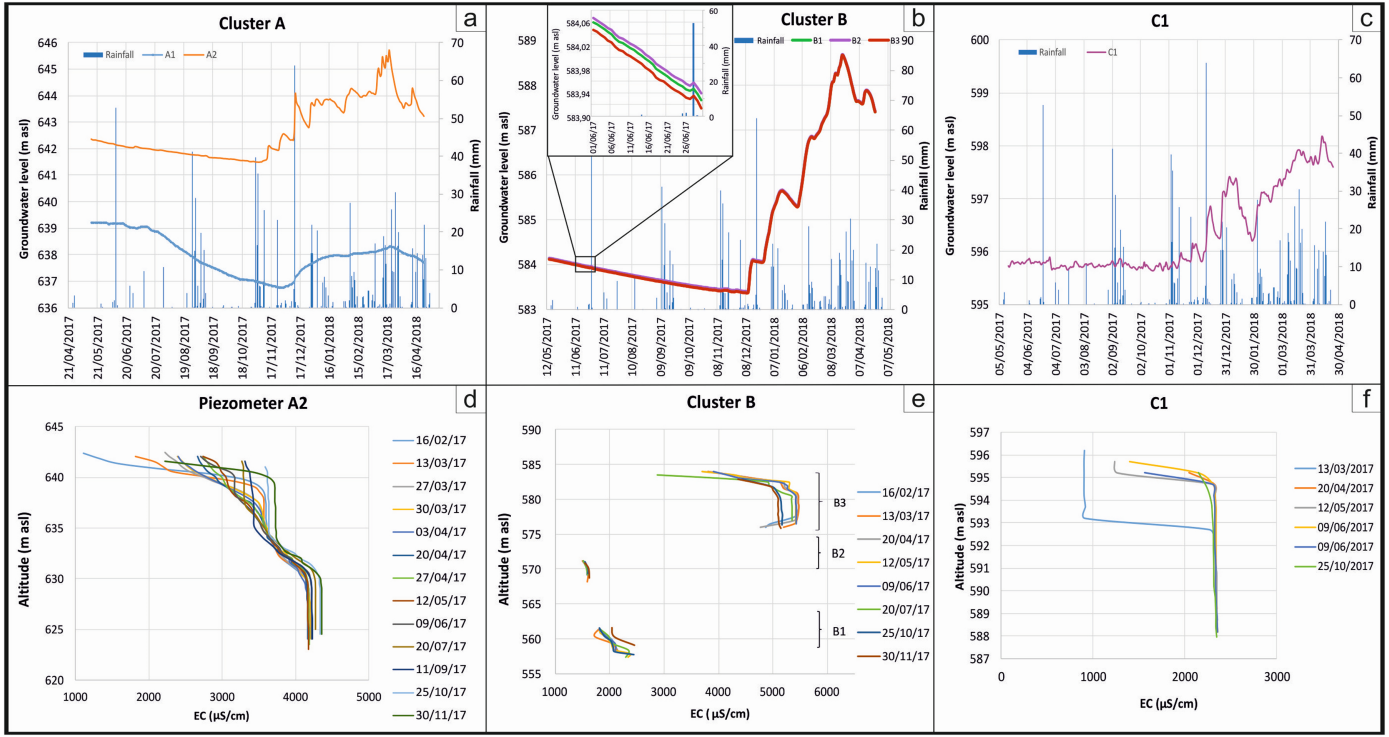
Cluster A
a
Rainfall
A1
A2
Groundwater level (m asl)
Rainfall (mm)
Cluster B
b
Rainfall
B1
B2
B3
C1
c
Piezometer A2
d
Altitude (m asl)
EC (µS/cm)
16/02/17
13/03/17
27/03/17
30/03/17
03/04/17
20/04/17
27/04/17
12/05/17
09/06/17
20/07/17
11/09/17
25/10/17
30/11/17
e
B3
B2
B1
f

Figure 6

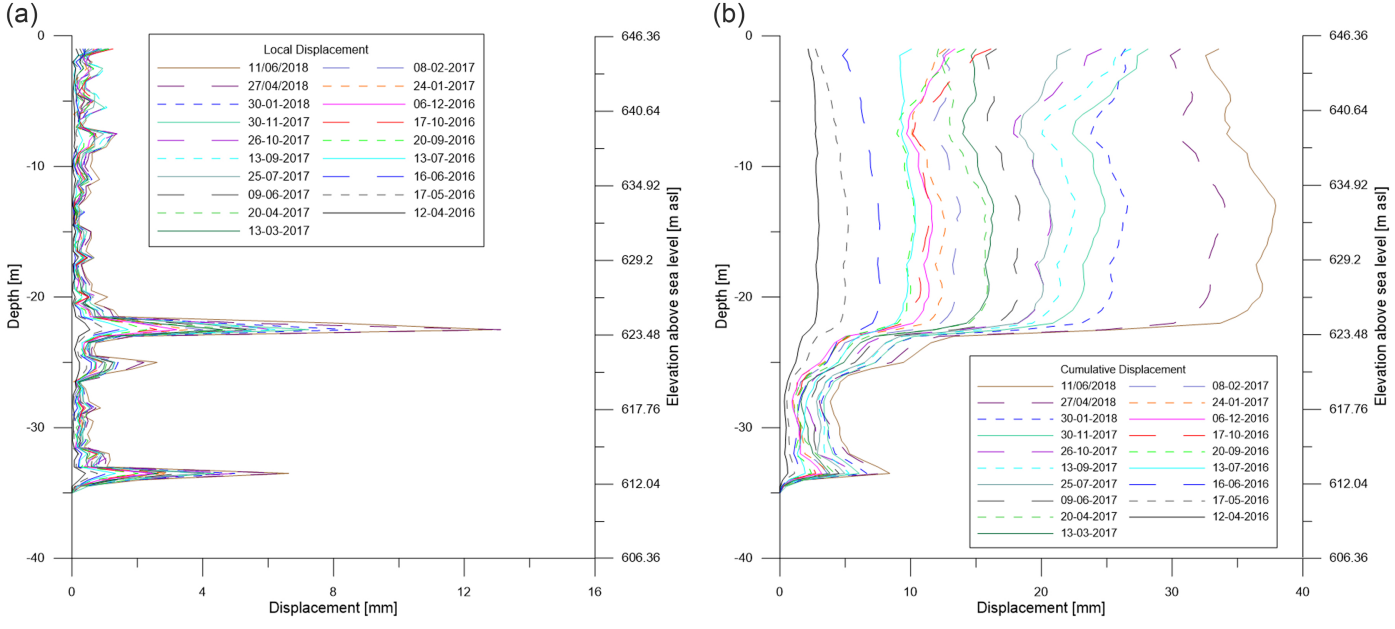
(a)
Local Displacement
11/06/2018
27/04/2018
30-01-2018
30-11-2017
26-10-2017
13-09-2017
25-07-2017
09-06-2017
20-04-2017
13-03-2017
08-02-2017
24-01-2017
06-12-2016
17-10-2016
20-09-2016
13-07-2016
16-06-2016
17-05-2016
12-04-2016
Depth [m]
0
-10
-20
-30
-40
Displacement [mm]
0
4
8
12
16
Elevation above sea level [m asl]
646.36
640.64
634.92
629.2
623.48
617.76
612.04
606.36
(b)
Cumulative Displacement
11/06/2018
27/04/2018
30-01-2018
30-11-2017
26-10-2017
13-09-2017
25-07-2017
09-06-2017
20-04-2017
13-03-2017
08-02-2017
24-01-2017
06-12-2016
17-10-2016
20-09-2016
13-07-2016
16-06-2016
17-05-2016
12-04-2016
Depth [m]
0
-10
-20
-30
-40
Displacement [mm]
0
10
20
30
40
Elevation above sea level [m asl]
646.36
640.64
634.92
629.2
623.48
617.76
612.04
606.36

Figure 7

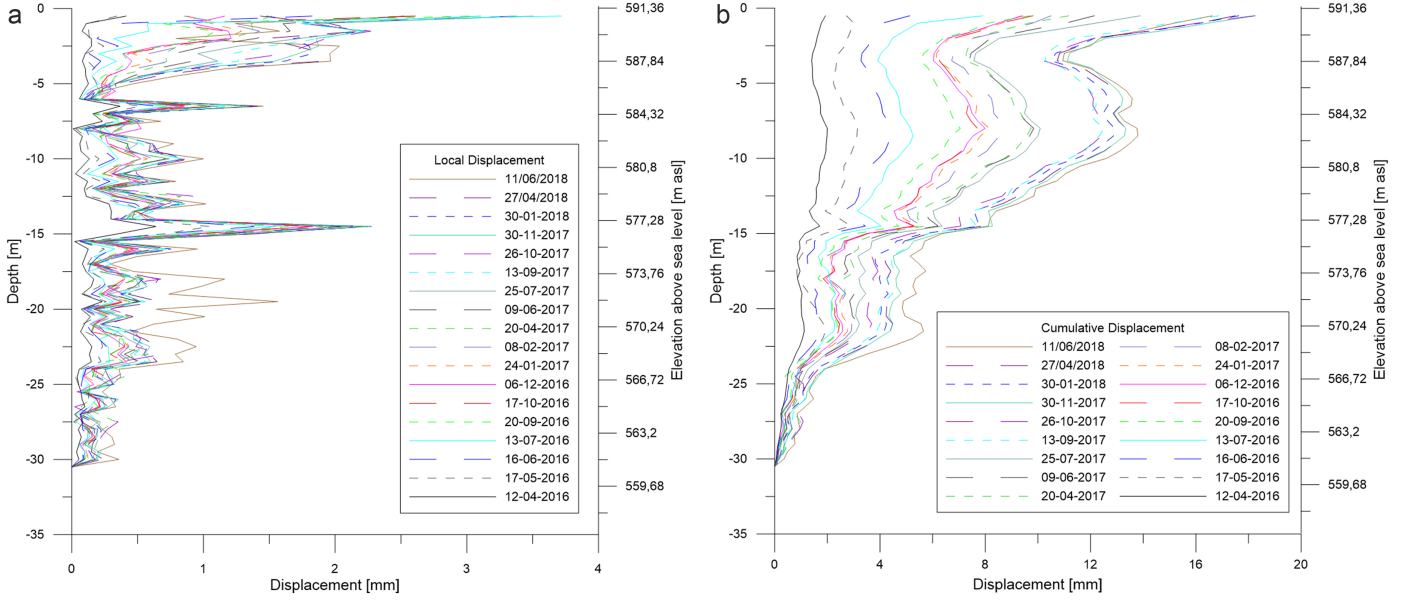
a
Depth [m]
0
-5
-10
-15
-20
-25
-30
-35
Displacement [mm]
0
1
2
3
4
Elevation above sea level [m asl]
591,36
587,84
584,32
580,8
577,28
573,76
570,24
566,72
563,2
559,68
Local Displacement
11/06/2018
27/04/2018
30-01-2018
30-11-2017
26-10-2017
13-09-2017
25-07-2017
09-06-2017
20-04-2017
08-02-2017
24-01-2017
06-12-2016
17-10-2016
20-09-2016
13-07-2016
16-06-2016
17-05-2016
12-04-2016
b
Depth [m]
0
-5
-10
-15
-20
-25
-30
-35
Displacement [mm]
0
4
8
12
16
20
Elevation above sea level [m asl]
591,36
587,84
584,32
580,8
577,28
573,76
570,24
566,72
563,2
559,68
Cumulative Displacement
11/06/2018
27/04/2018
30-01-2018
30-11-2017
26-10-2017
13-09-2017
25-07-2017
09-06-2017
20-04-2017
08-02-2017
24-01-2017
06-12-2016
17-10-2016
20-09-2016
13-07-2016
16-06-2016
17-05-2016
12-04-2016

Figure 8

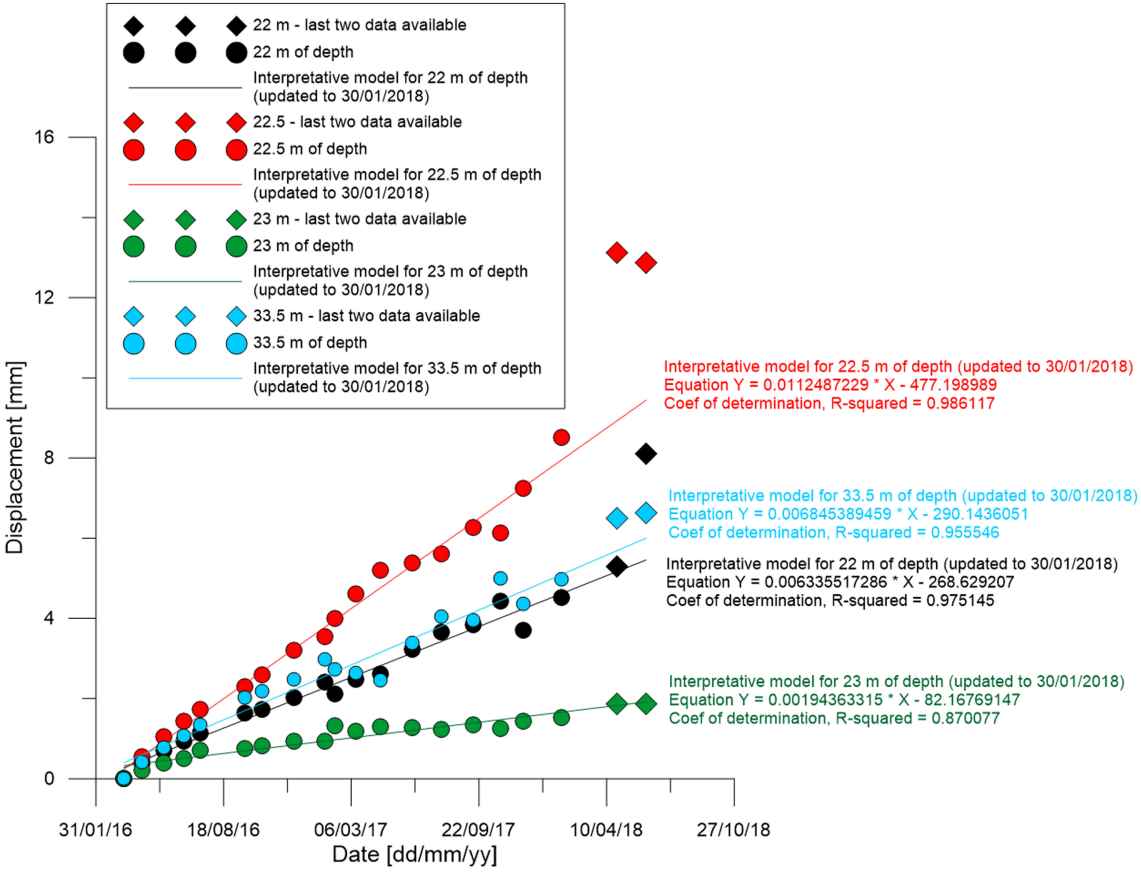
22 m - last two data available
22 m of depth
Interpretative model for 22 m of depth (updated to 30/01/2018)
22.5 - last two data available
22.5 m of depth
Interpretative model for 22.5 m of depth (updated to 30/01/2018)
23 m - last two data available
23 m of depth
Interpretative model for 23 m of depth (updated to 30/01/2018)
33.5 m - last two data available
33.5 m of depth
Interpretative model for 33.5 m of depth (updated to 30/01/2018)
Interpretative model for 22.5 m of depth (updated to 30/01/2018)
Equation Y = 0.0112487229 * X - 477.198989
Coef of determination, R-squared = 0.986117
Interpretative model for 33.5 m of depth (updated to 30/01/2018)
Equation Y = 0.006845389459 * X - 290.1436051
Coef of determination, R-squared = 0.955546
Interpretative model for 22 m of depth (updated to 30/01/2018)
Equation Y = 0.006335517286 * X - 268.629207
Coef of determination, R-squared = 0.975145
Interpretative model for 23 m of depth (updated to 30/01/2018)
Equation Y = 0.00194363315 * X - 82.16769147
Coef of determination, R-squared = 0.870077
Displacement [mm]
16
12
8
4
0
31/01/16
18/08/16
06/03/17
22/09/17
10/04/18
27/10/18
Date [dd/mm/yy]

Figure 9

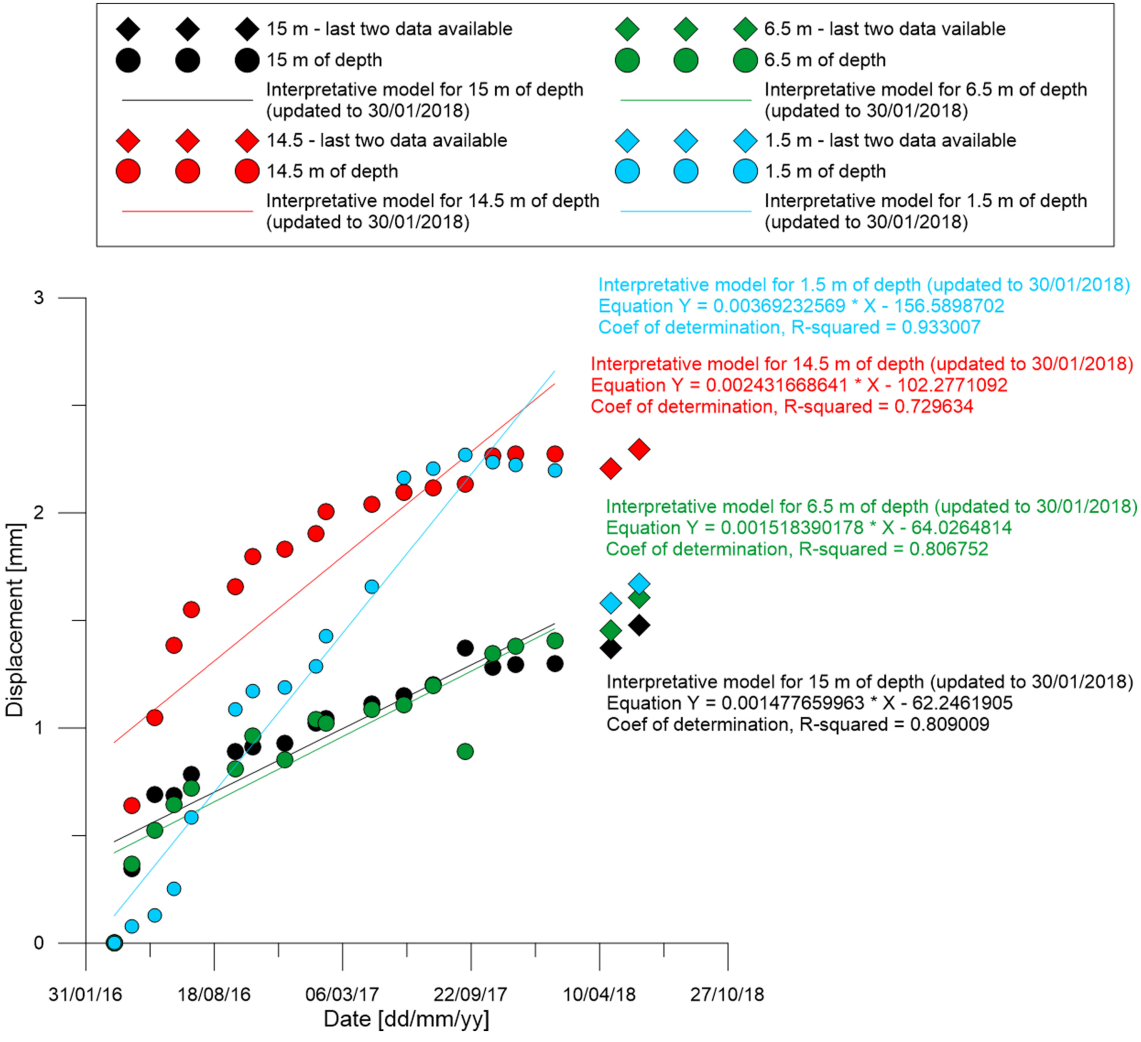
15 m - last two data available
15 m of depth
Interpretative model for 15 m of depth (updated to 30/01/2018)
14.5 - last two data available
14.5 m of depth
Interpretative model for 14.5 m of depth (updated to 30/01/2018)
6.5 m - last two data vailable
6.5 m of depth
Interpretative model for 6.5 m of depth (updated to 30/01/2018)
1.5 m - last two data available
1.5 m of depth
Interpretative model for 1.5 m of depth (updated to 30/01/2018)
Interpretative model for 1.5 m of depth (updated to 30/01/2018)
Equation Y = 0.00369232569 * X - 156.5898702
Coef of determination, R-squared = 0.933007
Interpretative model for 14.5 m of depth (updated to 30/01/2018)
Equation Y = 0.002431668641 * X - 102.2771092
Coef of determination, R-squared = 0.729634
Interpretative model for 6.5 m of depth (updated to 30/01/2018)
Equation Y = 0.001518390178 * X - 64.0264814
Coef of determination, R-squared = 0.806752
Interpretative model for 15 m of depth (updated to 30/01/2018)
Equation Y = 0.001477659963 * X - 62.2461905
Coef of determination, R-squared = 0.809009
Displacement [mm]
3
2
1
0
31/01/16
18/08/16
06/03/17
22/09/17
10/04/18
27/10/18
Date [dd/mm/yy]

Figure 10

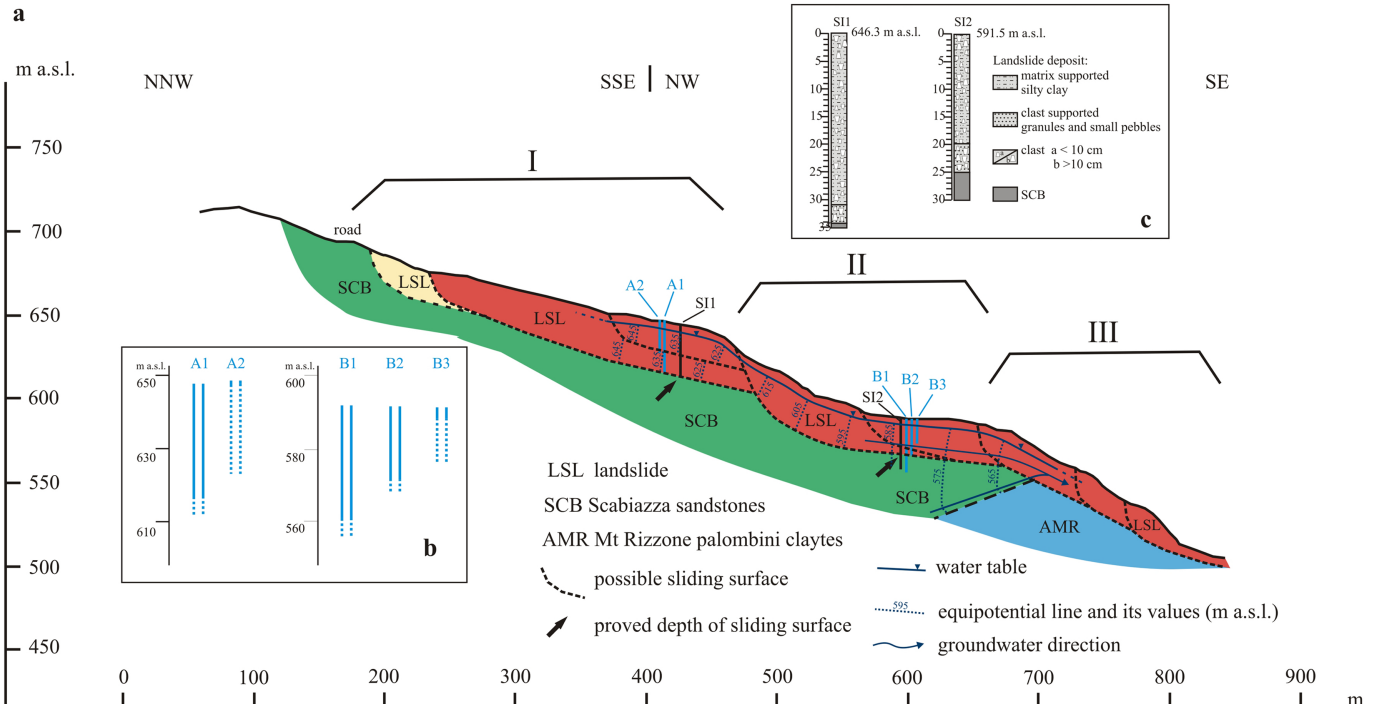
a
m a.s.l.
NNW
SSE | NW
SE
750
700
650
600
550
500
450
0
100
200
300
400
500
600
700
800
900
m
I
II
III
road
SCB
LSL
A2
A1
SI1
B1
B2
B3
SI2
AMR
LSL landslide
SCB Scabiazza sandstones
AMR Mt Rizzone palombini claytes
possible sliding surface
proved depth of sliding surface
water table
equipotential line and its values (m a.s.l.)
groundwater direction
b
c
SI1 646.3 m a.s.l.
SI2 591.5 m a.s.l.
Landslide deposit:
matrix supported silty clay
clast supported granules and small pebbles
clast a < 10 cm
b >10 cm

Figure 11

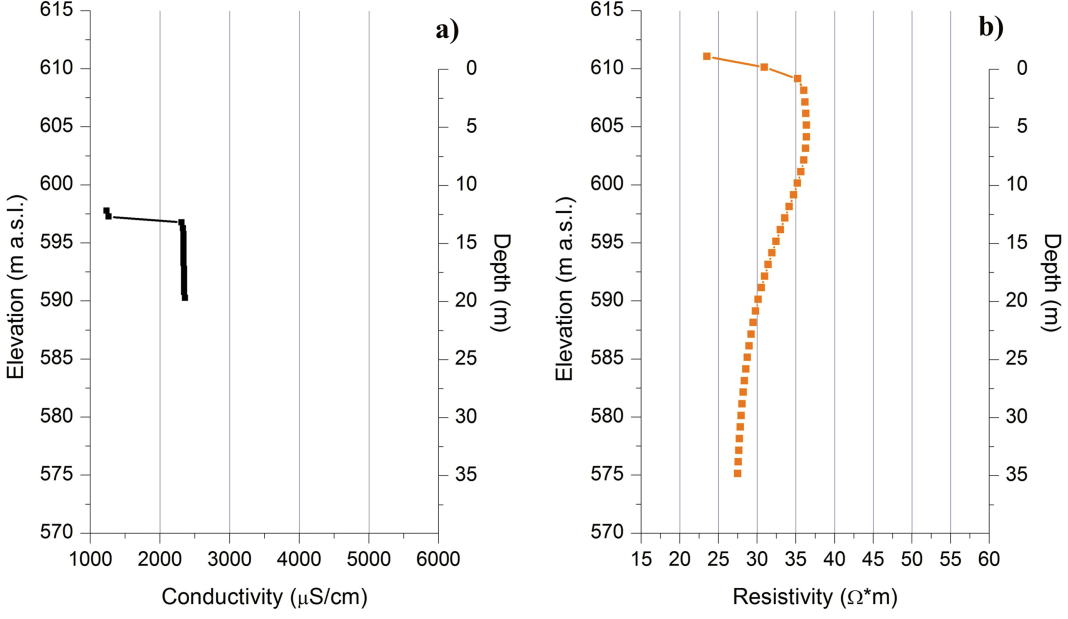
a)
b)
Elevation (m a.s.l.)
Depth (m)
Conductivity (μS/cm)
Resistivity (Ω*m)
615
610
605
600
595
590
585
580
575
570
0
5
10
15
20
25
30
35
1000
2000
3000
4000
5000
6000
15
20
25
30
35
40
45
50
55
60

Figure 12

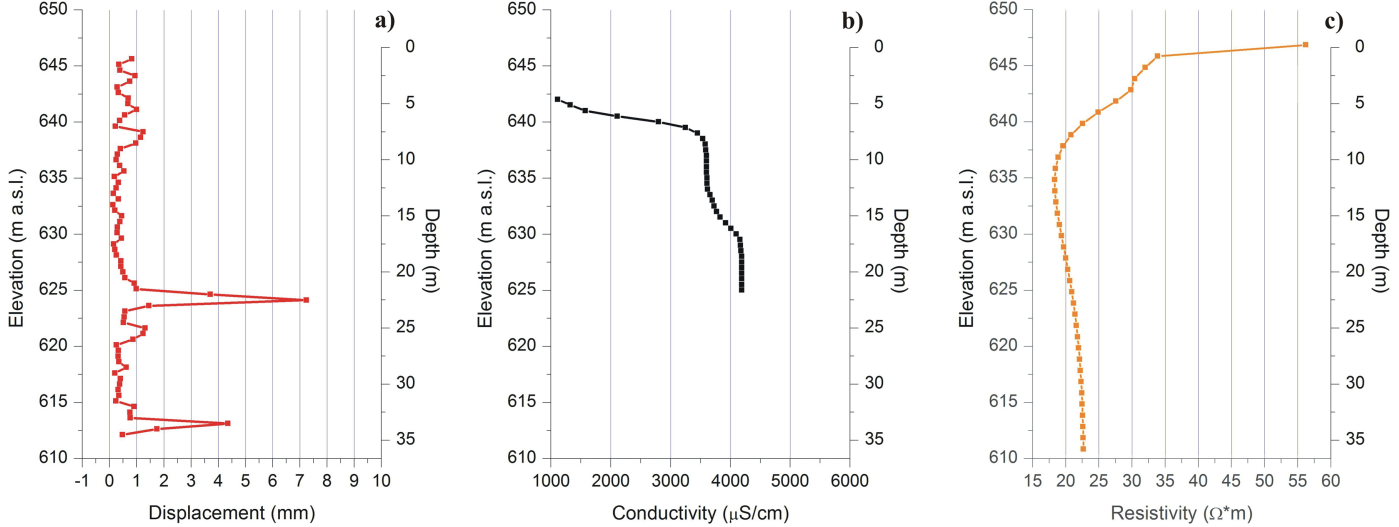
a)
b)
c)
Elevation (m a.s.l.)
Depth (m)
Displacement (mm)
Conductivity (μS/cm)
Resistivity (Ω*m)

Figure 13

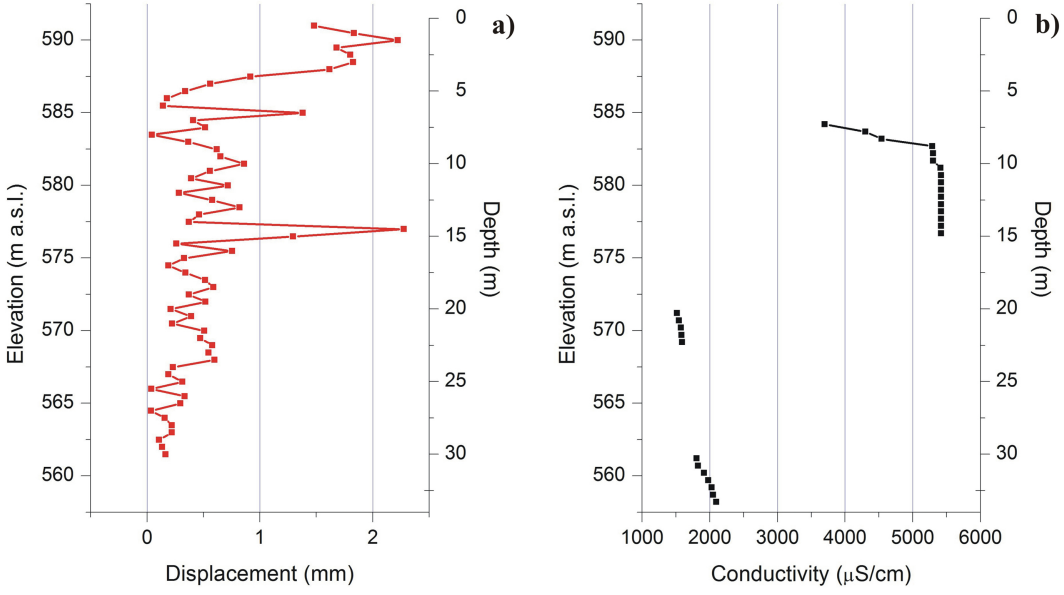
a)
b)
Elevation (m a.s.l.)
Depth (m)
Displacement (mm)
Conductivity (μS/cm)
590
585
580
575
570
565
560
0
5
10
15
20
25
30
1
2
1000
2000
3000
4000
5000
6000

Figure 14